MEASUREMENT OF D^0 DIRECTED FLOW AND ELLIPTIC FLOW IN AU+AU COLLISIONS AT $\sqrt{s_{\mathrm{NN}}} = 200$ GEV

A Dissertation

Submitted to the Faculty

of

Purdue University

by

Liang He

In Partial Fulfillment of the

Requirements for the Degree

of

Doctor of Philosophy

May 2019

Purdue University

West Lafayette, Indiana

THE PURDUE UNIVERSITY GRADUATE SCHOOL
STATEMENT OF DISSERTATION APPROVAL

Dr. Fuqiang Wang, Chair

      Department of Physics and Astronomy

Dr. Denes Molnar

      Department of Physics and Astronomy

Dr. Rafael F. Lang

      Department of Physics and Astronomy

Dr. Wei Xie

      Department of Physics and Astronomy

Approved by:

      Dr. John P. Finley

        Head of the Department of Physics and Astronomy

ACKNOWLEDGMENTS

First, I would like to express my sincere gratitude to my advisor Prof. Fuqiang Wang for his continuous support of my Ph.D study and related research, for his patience, innovation ideas, and immerse knowledge. His guidance helped me in all the time of research and attitude to the world. I could not have imagined having a better advisor and mentor for my Ph.D study. I would also like to thank Prof. Wei Xie for this close supervision in my first experimental research. His insightful comments and encouragement helped me to be a good member of the collaboration. I would also like to express my appreciation to Dr. Jie Zhao for the technique supports and the discussions with him. I am truly indebted to Prof. Denes Molnar for the valuable and fun discussion with him. I also would like to thank Prof. Rafael Lang for serving on my thesis committee.

Besides my thesis committee, I would like to thank my fellow graduate students in heavy-ion group for our daily discussions: Mustafa Mustafa, Li Yi, David Garand, Jian Sun, Kurt Jiang, Deke Sun, Lingshan Xu, Kun Jiang, Liang Zhang, Cheng-Chieh Peng, Terrence Edmonds, Rui Xiao, Hao Qiu, Yicheng Feng, An Gu. With a special mention to Dr. Xin Dong for his guidance in making me a good team player of STAR collaboration. My sincere thanks also goes to Dr. Chen Chen, David Zhao, Dr. Shiyan Wang, Xuhui Zhou for the friendship to support our living overseas.

Finally I would like to thank my mother Shuying Chang and my father Yuchun He, who have provided me through moral and emotional support in my life. I am also grateful to my fiance Jingru Wang for her supports and accompany along the way.

Thanks for all your encouragement!

TABLE OF CONTENTS

LIST OF TABLES

LIST OF FIGURES

Figure   Page

ABSTRACT

He, Liang Ph.D., Purdue University, May 2019. Measurement of D^0 Directed Flow and Elliptic Flow in Au+Au Collisions at $\sqrt{s_{NN}} = 200$ GeV . Major Professor: Fuqiang Wang.

A strongly interacting Quark Gluon Plasma (QGP) is created in relativistic heavy ion collisions at the Relativistic Heavy Ion Collider (RHIC). Owning to their large mass, charm quarks are produced by initial parton-parton hard scatterings and experience the entire evolution of the QGP medium created in heavy ion collisions. They can therefore be a valuable tool to study the early time dynamics and the properties of the QGP. Many experimental observables are exploited to extract the information of QGP. This thesis analyzes the directed flow (v_1) and the elliptic flow (v_2) of D^0 mesons (carrying a charm quark) using data collected by the Heavy Flavor Tracker in the STAR experiment in 2014 and 2016 RHIC runs. The v_1 and v_2 are measured by the first and second order Fourier coefficients of the D^0 azimuthal distribution relative to the reaction plane. The measurements help constrain the parameters in theoretical models to describe heavy quark dynamics in the QGP. The measurements are compared to the $v_1(2)$ of light flavors to shed additional insights on the QGP.

1. INTRODUCTION

1.1 Quark Gluon Plasma

1.1.1 Quark Model

In the year 1964, the quark model was introduced by Murray Gell-Mann [1] and George Zweig [2] (independently). A quark is a elementary particle and a fundamental constituent of matter. Hadrons are composite particles combined by quarks. Hadrons include mesons and baryons. The mesons are constructed from one quark and one anti-quark and the baryons by three quarks. The quarks were experimentally discovered in 1968 by Deep-Inelastic-Scattering (DIS) experiments [3]. The electron proton scatterings at Stanford Linear Accelerator Center (SLAC) showed point structures as deflection centers. The point structures have fractional charges and were named "partons" by Feynman [4]. The concept of "color" was introduced to explain apparent violation of the Pauli exclusion principle caused by the discovering spin–3/2 baryons, which have 3 up quarks with sligned spins [5]. The additional color degree-of-freedom was formalized to carry the three fermions form of a spin–3/2 ground state. The color charge defines a SU(3) symmetry which is used to describe the Quantum Chromodynamics (QCD).

1.1.2 Quantum Chromodynamics

Quantum Chromodynamics (QCD) [6] is a non-abelian quantum field theory that describes the strong interaction between quarks and gluons based on a local SU(3) symmetry. The QCD Lagrangian is:

$$\mathcal{L}_{QCD} = -\frac{1}{4} \sum_{gluons} G^a_{\mu\nu} G_a^{\mu\nu} + \sum_{flavors} \bar{\psi}_i (i\gamma^\mu D_\mu - m)\psi_i \qquad (1.1)$$

The meanings of each term are:

- i denotes to the index of flavors;

- α denotes to the index of gluons;

- ψ_i are quark Dirac spinor fields;

- $G^a_{\mu\nu}$ are gluon fields strength tensor;

- $D_\mu = \partial_\mu - igA_{(\mu)}(x)$ is the gauge covariant derivative, where $A_\mu(x)$ is gluon gauge fields and g is the coupling constant of the strong force [7].

The non-linear term in the field strength tensor $G^a_{\mu\nu}$ differs QCD from QED. This term makes QCD a "local" SU(3) theory.

The fine structure constant α_s depends on scale as [8]:

$$\alpha_s(Q) = \frac{\alpha_s}{1 + (11n - 2n_f)(\alpha_s/6\pi)ln(Q/\mu)} \tag{1.2}$$

where n is the number of colors ($n = 3$ for QCD); n_f is the number of quark flavors, which equals to 6 in SU(3); $\mu = \Lambda_{QCD} \approx 200 MeV$ is the scaling parameter. For very large momentum transfer Q or very short distances the coupling constant can be written as

$$\alpha_s(Q) \approx \frac{2\pi}{(11 - \frac{2}{3}n_f)ln(Q/\Lambda_{QCD})} \tag{1.3}$$

which is called asymptotic freedom of QCD. As $Q \to \infty$, $\alpha_s \to 0$. When the interaction is weak, perturbative techniques can be applied. Assuming the world average $\alpha_s(M_z) = 0.1184 \pm 0.0007$ [9], perturbative QCD is valid at $Q \approx 90$ GeV. Perturbative QCD is a good tool at high energies and short range interactions [10, 11]. For large–Q partonic collisions, perturbative techniques can be applied. Perturbative QCD is one of the most reliable tests of QCD. It is used to compare with experimental data.

In long–distance interactions, QCD is non-perturbative because its coupling constant is large. For example, a quark–antiquark pair color flux tubes confine the color field and limit

the distance between quark and anti-quark to about $1fm \approx 1/\Lambda$(typical hadron size). The QCD wave function of hadrons cannot be solved analytically. With the help of supercomputers, lattice QCD has been a mature approach to solve QCD numerically [9,12]. In lattice QCD, the space-time is segmented on lattice grids. The quark fields are defined at the grid points; the gluon fields are defined on links between grid path. Lattice QCD becomes more accurate if one makes the lattice space smaller. Lattice QCD has been proved to be the most reliable tool to explain non-perturbative QCD.

1.1.3 Quark Gluon Plasma

When the temperature or baryon density of nuclear matter is high enough, the matter exists in the form of the QGP [13–16], where the partons are not confined into hadrons. The QGP can be treated as relativistic gas. For a relativistic gas, the energy density is

$$\epsilon = (g_b + \frac{7}{8}g_f)\frac{\pi^2}{30}T^4 \tag{1.4}$$

Here g_b and g_f are the degree of freedom for bosons and fermions, respectively. Both bosons and fermions are assumed to be massless. For relativistic gas, pressure $P = \epsilon/3$ and entropy $s = (4/3)(\epsilon/T)$. Gluons come in 8 different colors and 2 helicities, so $g_b = 8 \times 2 = 16$. Quarks have 3 colors, 2 charge states (quark and anti–quark) and 2 spin states. If we consider only up and down quarks, then $g_f = 3 \times 2 \times 2 \times 2 = 24$.

QGP can be created by heavy-ion collisions. We can understand QGP as a fluid of quarks and gluons. The QGP is the hottest, densest form of matter with lowest viscosity created in the laboratory. The strongly-coupled QGP is sometimes called 'perfect liquid' due to its super low viscosity.

1.2 Heavy-Ion Collision

QGP is believed to have existed in the early stage of our universe, about a few tens of microseconds after the big bang. Heavy-ion collisions are the only way to create the QGP

in laboratory. The two major facilities for this are Relativistic Heavy Ion Collider (RHIC) (BNL, USA) and the Large Hadron Collider (LHC) (CERN, Switzerland). RHIC started to operate in the year 2000. It provides collisions to the PHENIX and STAR experiments, and also two other smaller experiments BRAHMS and PHOBOS. In the year 2005, the four experiments jointly announced the discovery of the QGP [13–16]. The results showed that the QGP is a phase in $Au + Au$ collisions at RHIC highest beam energy $\sqrt{s_{\text{NN}}} = 200 GeV$. The LHC was running $Pb + Pb$ collisions since the year 2010 at larger beam energies than at RHIC. As a result, the initial temperature of heavy-ion collisions at the LHC is higher than at RHIC. Results from the LHC confirmed findings at RHIC about properties of QGP [17, 18]. The heavy-ion collisions were initially expected to be weakly coupled. However, the ideal hydrodynamics can be used to describe the bulk observables from RHIC. This suggests that the matter is a low viscosity QGP phase. This finding of RHIC indicates a strongly-interacting quark-gluon plasma (sQGP) [19].

Figure 1.1 shows the phase diagram of nuclear matter. The x-axis is baryochemical potential, which is the potential energy to put one baryon into the system. The y-axis is the temperature in MeV. At lower temperatures and lower baryochemical potentials, we have a hadron gas mainly made of pions. At higher temperatures, we have the QGP.

In heavy-ion collisions, the two ions initially have pancake shapes due to their high momenta. At high energy the wavefunctions are dominated by gluons with small longitudinal momentum. This state is modeled by the Color-Glass Condensate (CGC) theory [21]. We can roughly consider the heavy-ion collision as comprised of three stages. The first stage is collision between two big gluonic balls. The second stage is a near-zero viscosity partonic scattering phase, including the QGP phase. The quarks and gluons expand and interact in this stage. The third stage is the hadronic re-scattering stage. At the early time of the partonic phase, the mean free path of the system is short. The system can be described by ideal hydrodynamics. Then the energy density drops and the medium starts to hadronize. The abundances of particles are first fixed, which is called chemical freeze-out. When the mean free path is larger than the size of system, the interaction between hadrons stops. This stage is called kinetic freeze-out [19].
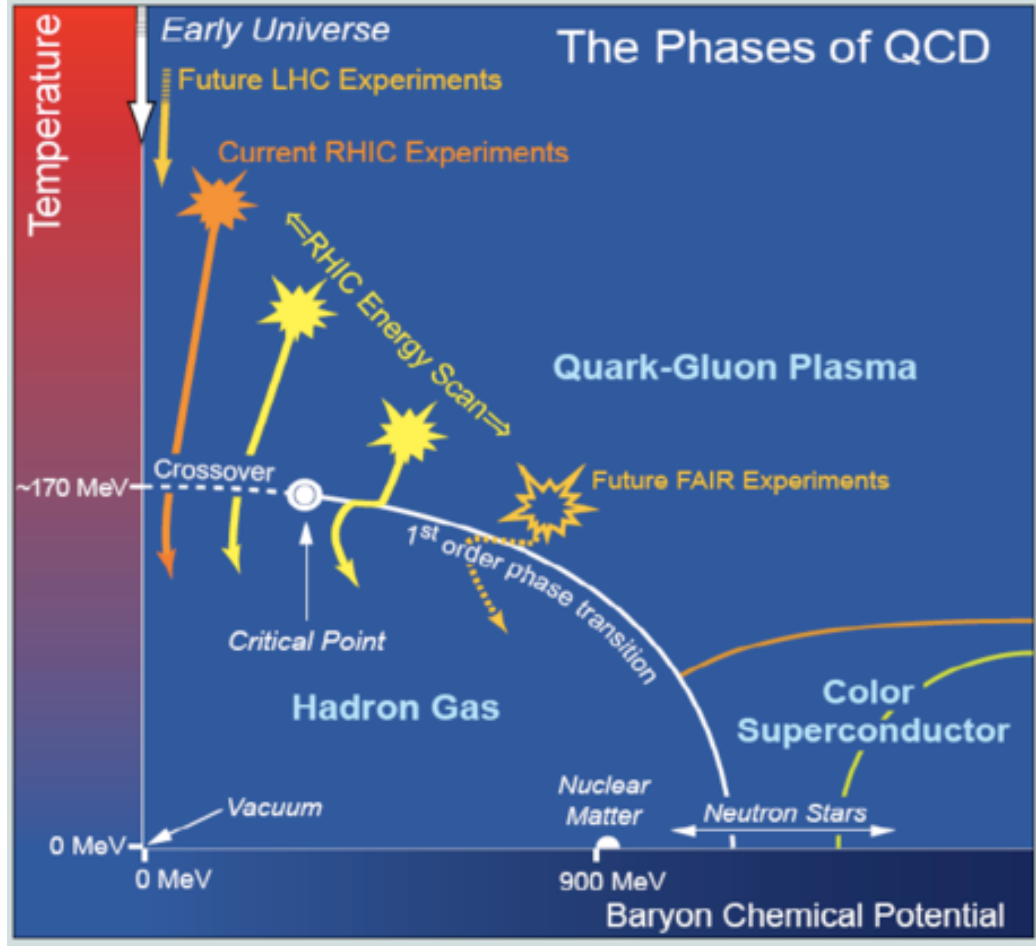
Figure 1.1. The phase diagram of nuclear matter [20].

1.3   Open Heavy Flavor Measurements

1.3.1   Heavy Quarks as Probes of sQGP

To study sQGP, heavy quarks (charm and bottom quarks) are used as probes. The heavy quarks are good probes for sQGP for several reasons, which are based on $m_Q \gg T_C$ (critical temperature), Λ_{QCD} [22]:

- Heavy quarks are produced by hard processes. The production of heavy quarks happens in early stage of medium.

- The thermalization time, which is proportional to m_Q/T, of heavy quarks is late than bulk (with thermalization time is about to be 0.5 fm/c). Considering lifetime of QGP at RHIC is about to be 5fm/c, the heavy quarks might not be fully thermalized in QGP. So that heavy quarks are good probe because they retain memory of the interaction in sQGP.

- Bremsstrahlung of an accelerated charged particle is suppressed by a factor of $(m_{light}/m_{heavy})^4$ for heavy quarks. Compared with elastic scattering, the contribution from gluon radiation of heavy quarks is much suppressed.

- In the nonrelativistic approximation, $p_Q^2/2m_Q \approx 3T/c$, for heavy quarks. If $p \gg T$, $p_Q^2 \approx m_Q T \gg T^2$, $i,e.$ the momentum transfer from the thermal medium to heavy quark is small compared to the quarks. For this reason, a Brownian motion approach can be applied to describing the heavy quarks in sQGP.

Open heavy flavor hadrons have a (short) decay length. So, ideally we can identify the decay products of heavy hadrons and reconstruct them in experiments. But this is still hard to do in practice because in the reconstruction with large combinatorial background. Nevertheless, one can succeed with the help of the high tracking resolution detector and topological cuts. In STAR at RHIC, the newly installed Heavy Flavor Tracker (HFT) with resolution $\sim 40\mu m$ can help reconstruct the secondary vertex, because the open heavy flavor hadron decays with decay length $\sim 100\mu m$.

1.3.2 D^0 Directed Flow (v_1) and Elliptic Flow (v_2)

Collective flow is an important property that can be used to understand QGP. In heavy-ion collisions, the spatial anisotropy will get translated to a final momentum anisotropy. We can study the azimuthal event shapes in momentum space by the azimuthal anisotropy, which is defined as the particle yield in Fourier series around the reaction plane azimuth Ψ_{rp}:

$$E\frac{d^3N}{dp^3} = \frac{d^2N}{2\pi p_T dp_T dy}(1 + \sum(2v_n \cos[n(\phi - \Psi_{rp})])), \qquad (1.5)$$

$$v_n = \langle \cos[n(\phi - \Psi_{rp})] \rangle \tag{1.6}$$

In the expansion, v_1 is called directed flow, while v_2 is called elliptic flow.

v_1 is the magnitude of the total vector sum of the transverse momenta. It is due to the pressure built up between nuclei during the time of overlap of the two collectivities. The v_1 is established at a very early stage, so it is a sensitive probe into the early time dynamics of the heavy-ion collisions [23–25]. A hydrodynamic calculation with a tilted initial source [26] can explain the negative slope of v_1 as a function of rapidity or "anti-flow" of charged hadrons measured at RHIC energies at midrapidity [27]. Recently a framework, based on Langevin dynamics for heavy quarks coupled to a hydrodynamic background calculation has predicted a stronger v_1 for the D mesons to light hadrons [28]. The measurement of the D meson v_1 can hence be used to constrain the drag coefficients of the tilted bulk system. Furthermore, a larger v_1 for heavy quarks is predicted to result from the transient magnetic field generated in heavy-ion collisions. The sign of v_1 induced by the initial electromagnetic field is predicted to be opposite for charm and anti-charm quarks, although the magnitude of the resulting v_1 splitting may be smaller than the overall v_1 induced by the drag from the tilted source [29, 30]. Thus, the v_1 splitting for D^0 and $\bar{D}^0$ may provide insights into the early-time electromagnetic field generated in heavy-ion collisions.

The v_2 presents the difference between the major and minor axis. The v_2 is build up by the transverse pressure gradient caused by spacial anisotropy. The measurement of heavy quark v_2 can be studied into two regimes based on the energy of heavy quarks. In the low transverse momentum range, the v_2 of heavy quarks reveals the degree of bulk matter thermalization. As the mass of bottom quark is larger than that of the charm quark, the production of heavy quark in low p_T range is dominated by charm quark. The finite heavy quark v_2 at low p_T is a suggestion that the charm quark interacts with medium strongly and frequently. In the high p_T ($p_T >$5GeV/c) region, the v_2 of heavy quarks is to be due to path length dependence of energy loss. To compare with different energy loss models, the measurements of heavy quarks at high p_T can give us insights into the mechanics of the energy loss.

2. EXPERIMENTAL SETUP

The work in this thesis is conducted with $Au + Au$ data taken by STAR [31] detector at RHIC accelerator.

2.1 Relativistic Heavy Ion Collider

RHIC (Relativistic Heavy Ion Collider) locates at Brookhaven National Laboratory (BNL) in Upton, New York. RHIC conducts different species of ions with very wide beam energy range. Figure 2.1 shows an aerial view of the RHIC facility. RHIC has a 3.8 km intersection storage ring with six interaction points. For heavy-ion programs, RHIC has successfully collided $p+p$, $d+Au$, $Cu+Cu$, $Cu+Au$, $Au+Au$ and $U+U$ with different beam energies. RHIC has also run beam energy scan of $Au + Au$ collisions at different beam energies ranging from 7.7 GeV to 200 GeV for the searching of a QCD critical point. Except for the heavy-ion programs, RHIC is also the only high energy polarized-proton collider in the world. The polarized protons collisions is set for spin physics to study the structure of the nucleon.

2.2 STAR detector

STAR (Solenoidal Tracker At RHIC) is located at one of the intersection point of RHIC ring. STAR is a multi-purpose detector. Its main purpose is to detect event-by-event high occupancy heavy-ion collisions. Figure 2.2 shows a cutaway side view of the STAR. STAR covers mid-rapidity and full azimuth. In the coverage, STAR provides very good particle identification thanks to its subsystems in the STAR. The heart of STAR is the Time Projection Chamber (TPC). It has full azimuthal and approximate $|\eta| < 2.5$ in rapidity coverage. The conventional coordinate system at STAR uses the center of the TPC as the
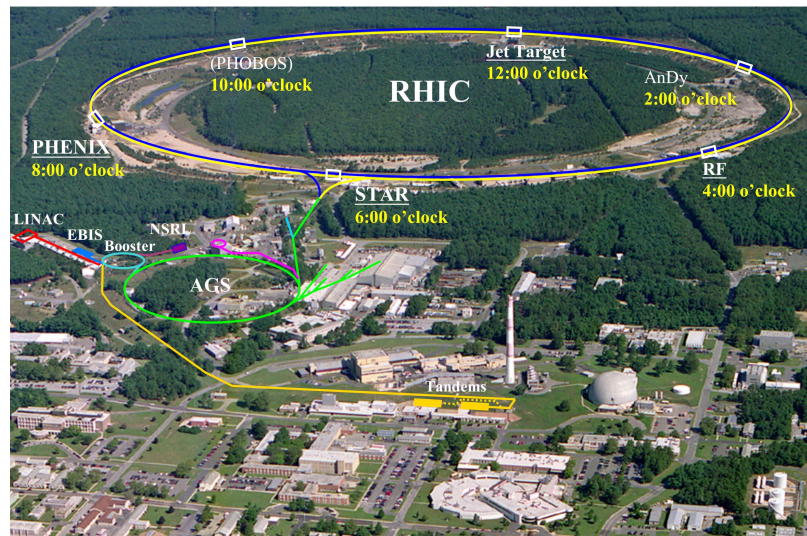
Figure 2.1. Aerial view of RHIC/AGS facility. The two principal experiments still running are PHENIX and STAR. The LINAC is the injector for polarized protons. The TANDEM is the injector for Ions. The dome is the decommissioned High Flux Beam Reactor while the enclosed ring on the lower right center is the National Synchrotron Light Source (NSLS). Figure modified from [32]

.
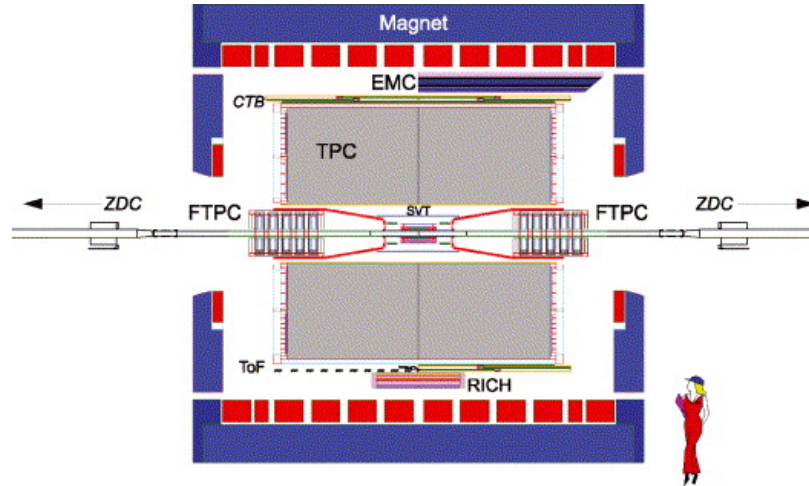
Figure 2.2. An illustration of a cutaway side view of the STAR detector. Figure modified from [31]

.

origin point. The beam pipe direction is defined as the z direction. The west direction is defined as positive. The x direction is pointing to the south and the y direction is pointing up.

2.2.1 Time Projection Chamber

The TPC (Time Projection Chamber) [33] is the most important part of STAR. It is a barrel detector filled with gas. TPC is 4 m in diameter and 4.2 m long. When the charged particles traverse in TPC, the particles ionize along their flying path. The released electrons drift to the TPC endcaps and are collected by the readout pads. The signal from readout is used to reconstruct the tracks of the particles. TPC can measure tracks momenta ranging from 150 MeV/c to 300 GeV/c. It can also identify pions and protons up to momentum $p \approx$ 1.1GeV/c; and kaons and pions up to about $p \approx 0.6$GeV/c, based on the ionization energy loss dE/dx.
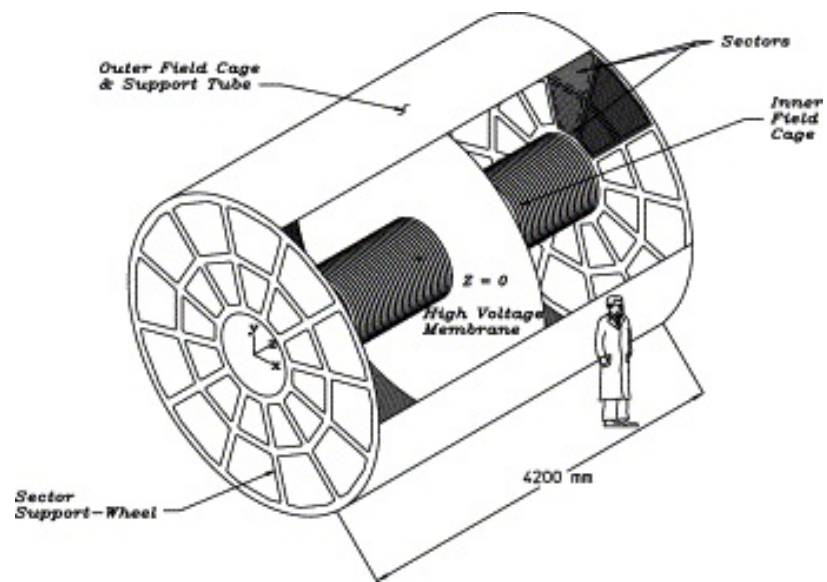
Figure 2.3. The illustration of the Time Projection Chamber(TPC) at STAR. Figure taken from [33]

.
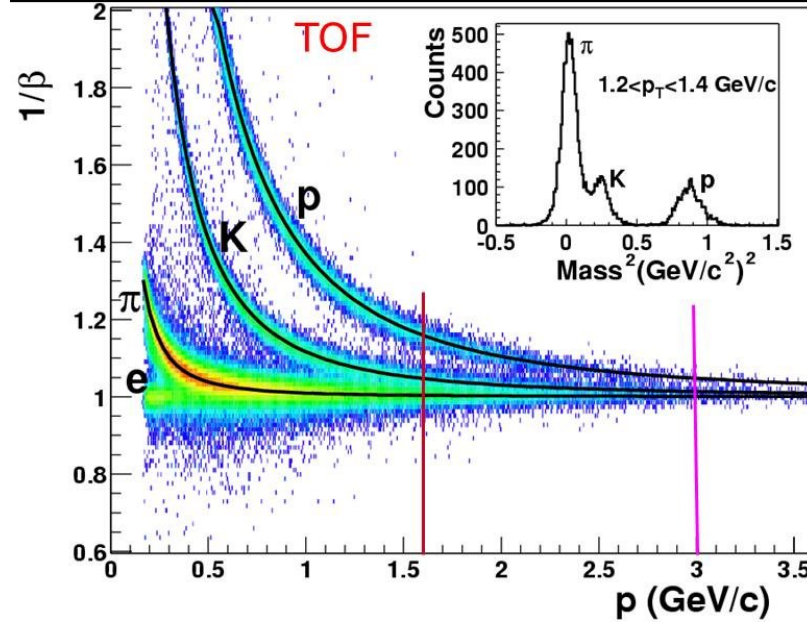
Figure 2.4. Particle identification provided by the Time of Flight (ToF) detector at STAR. Figure taken from [34].

2.2.2 Time of Flight detector

The ToF (Time-of-Flight) detector [34] is made of 120 trays MRPCs (Multigap Resistive Plate Chmbers). The ToF combines track hit timing information in MRPCs with timing of forward Vertex-Position-Detector (VPD) to calculate the flighting time of particles. ToF covers a pseudo-rapidity range $|\eta| < 0.9$ with full azimuth. The timing resolution of ToF is ~ 100 ps. The performance of ToF helps improving the particle identification. For π, K, p, the PID can be achieved up to $p \sim 1.7$-$1.9\mathrm{GeV}/c$ and for $(\pi + K), p$, up to about $|p| \sim$ 2.9–3.1 GeV/c.

2.2.3 Heavy Flavor Tracker

The HFT (Heavy Flavor Tracker) [35] is a relatively newly installed detector in STAR. It is a silicon detector located in the very central position of STAR constructed with three parts. From inner to outer, they are: Pixel Detector (two layers) with radius $\sim$2.8 and 8 cm, Inner Silicon Tracker (IST) at r = 14 cm, and Silicon Strip Detector (SSD) at r = 22
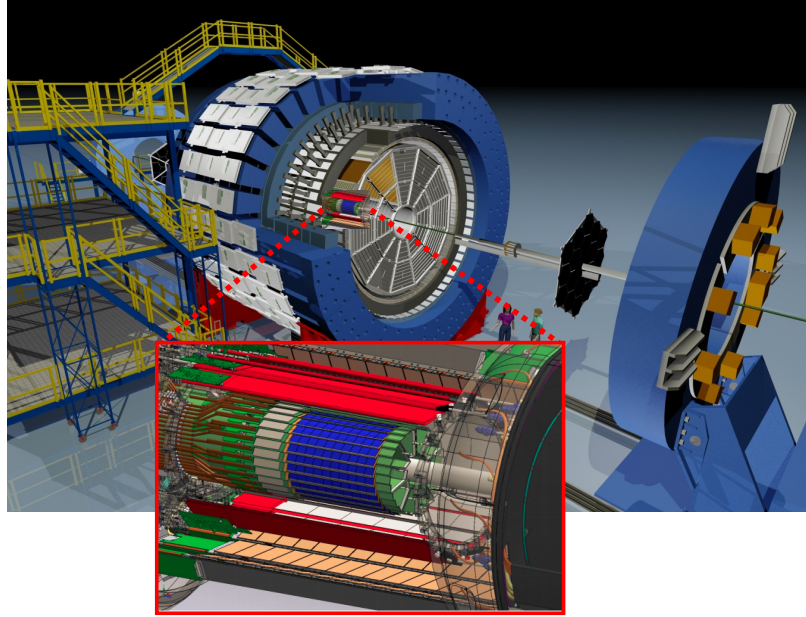
Figure 2.5. The illustration of the Heavy Flavor Tracker(HFT) at STAR.

cm. There are totally 8 layers in the HFT. The coverage rapidity range is $|\eta| < 1$ with full azimuth, which is the same as for the TPC. The resolution of the HFT can be as good as $< 30\mu$m for high momentum tracks. This high resolution makes it possible to reconstruct open heavy flavor particles topologically.

2.2.4   Zero Degree Calorimeter

The ZDCs (Zero Degree Calorimeters) [36] are two hadron calorimeters along the beam pipe. They measure the neutron energy after the charge particles bent out of the acceptance of the ZDC by the dipole magnets. ZDCs are located symmetrically at 18 meters away from the collision intersection point on each side. The horizontal acceptance is ± 5 cm. The signal timing difference between the two ZDCs also provides a measure of the collision location. The two main purposes of the ZDCs are event characterization and luminosity monitoring.
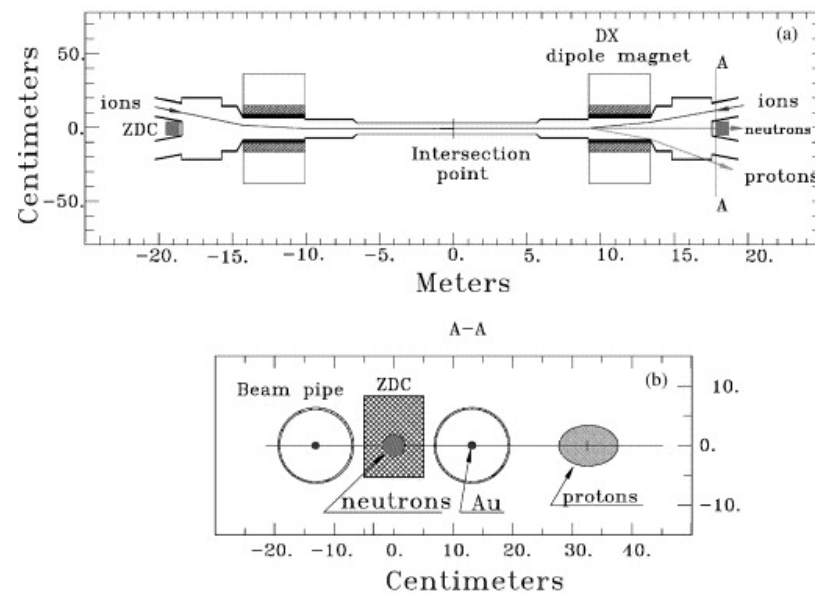
Figure 2.6. The illustration of the Zero Degree Calorimeter at STAR. Figure taken from [36].

2.3 Dataset

2.3.1 Centrality Definition

The impact parameter of a collision is the distance between the centers of the two colliding nuclei. A central collision with a zero impact parameter has a full overlap area, and tends to have the maximum energy density. A peripheral collision of two nuclei with large impact parameter has a small overlap zone, and tends to be similar to small system collisions. The systems generated from various initial collision geometries are different. The Glauber model is used to describe the collision geometry and link experimental observables with a theoretical impact parameter, the binary nucleon-nulceon collisions (N_{coll}) and the number of participating nucleons (N_{part}) [37]. The Glauber Monte Carlo model generates the nucleon distribution in the nuclei according to the Wood-Saxon density profile for different impact parameters. The Glauber model outputs the values of N_{coll} and N_{part}. In the experiments, the inclusive charged particle multiplicity is used for the centrality definition.

2.3.2 Dataset and Event Selection

The analysis in this thesis is based on Au+Au collisions at $\sqrt{s_{NN}}$=200 GeV collected by the STAR experiment during the 2014 and 2016 RHIC runs. The 2014 run was processed with P16id library, while the 2016 year run was processed with P16ij. In this analysis, we used picoDst files which is produced from MuDst.

In the analysis, minimum-bias trigger is used. For Run-14, it denoted as vpdmb-5-p-nobsmd (including run ID 450005, 450015, 450025) and vpdmb-5-p-nobsmd-hlt (450050, 450060). For the Run-16, it is denoted as VPDMB-5-p-sst (520001, 520011, 520021, 520031, 520041, 520051). These Run-14 and Run-16 analyses were done using "stphysics" stream data. In addition to that we have analyzed "stsst" and "stnosst" stream from production-2 of Run 16. The triggers used for these productions are "VPDMB-5-sst" (570001) and "VPDMB-5-nosst" (570002) for "stsst" and "stnosst" respectively. Since the HFT had a firmware problem during the year of 2014 and 2016 runs, certain run numbers have been

rejected from the analysis. For the 2014 dataset, the runs below day 107 are rejected, while for the 2016 data the run rejection condition was RunId > 17062047, $17065002 <=$ RunId $<= 17068053$ and $17063041 <=$ RunId $<= 17063043$. The following cuts are used to select good quality events:

- |primary vertex in z direction| < 6 cm

- |primary vertex in transverse direction| < 2 cm

- The difference of primary vertex to vpd in z direction $|PV_z \ vpdVz| < 3$ cm

- Exclude event with $PV_x < 10^{-5}$ and $PV_y < 10^{-5}$ and $PV_z < 10^{-5}$ at the same time.

The vpdVz is the vertex z position calculated from time difference measured by two sides of VPD. After cuts, there are about 870 M events remained in Run-14 and 1.06 B events in Run-16 for the "stphysics" stream. In addition, we had about 300 M and 100 M, respectively, events from the "stss" and "stnosst" streams in Run-16. So, in total, we have analyzed about 2.2 B good events.

A list of good runs is given in Ref. [38].

3. D^0 RECONSTRUCTION

In the analysis presented in this thesis, D^0s and $\bar{D}^0$s are reconstructed through the $K^\mp \pi^\pm$ channels for the full kinematics of the D mesons. In the following we will describe the daughter selection, the geometry cuts and how they are obtained through the Multivariate Data Analysis (TMVA) tuning. We will show the D^0 signals for different p_T bins. We will also discuss some related topics: the primary vertex reconstructed by the Kalman Filter algorithm with better quality than the STAR default, the mixed event to reconstruct the combinatorial background.

3.1 D^0 Decay and Geometrical Parameters

D^0 mesons have a decay length of 123 μm. In experiments, we identify the decay products of the heavy flavor hadrons and reconstruct them. The "golden" decay channels for D^0 mesons is $D^0 \rightarrow K^+ \pi^-$. The full kinematics of parent meson can be reconstructed by the K and π hadrons. The reconstruction of D^0 is possible by using topological cuts. This was made possible by the installation of the STAR secondary vertex tracker, the Heavy Flavor Tracker (HFT) [35].

The secondary vertex is reconstructed with selected K and π global tracks reconstructed by the TPC. The definitions of the topological cuts used in the analysis are shown in Fig. 3.1. Five geometrical variables are chosen to select D^0 and reject combinatorial background, which is dominated by a pair of tracks directly from the primary vertex (PV): 1)decay length (the distance between the decay vertex and PV), 2)DCA between the two daughters, 3)DCA between the reconstructed D^0 path and PV, 4)DCA between the π track and PV, and 5)DCA between the K track and PV. The cuts on these variables are optimized by the Toolkit for Multivariate Data Analysis (TMVA) package. These topological cuts vary in different D^0 candidate p_T region and centrality bins in order to have the best sig-

nificance. Additionally there is a $\cos(\theta) > 0$, where θ denotes the pointing angle between PV and the secondary vertex, cut to ensure the decay vertex relative to the primary vertex is roughly in the same direction.
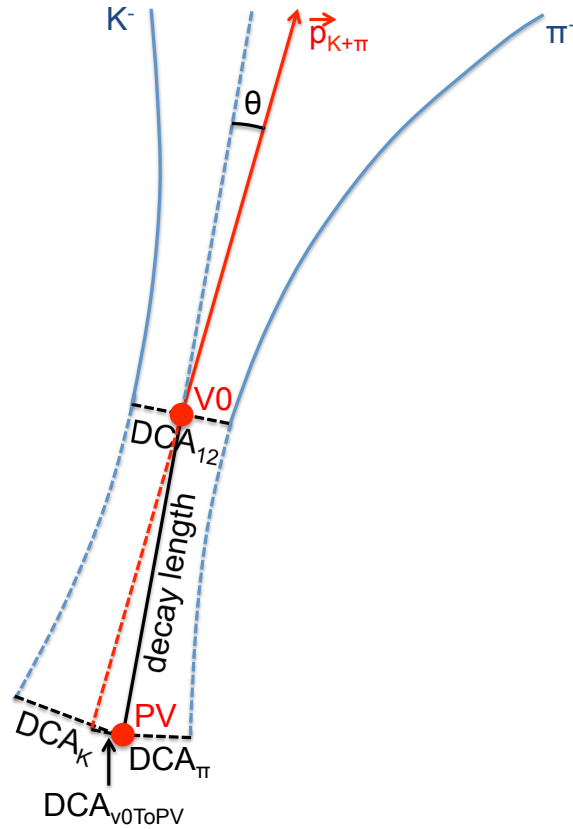
Figure 3.1. D^0 decay topological variables.

3.2 Pion and Kaon Particle Identification

For the D^0 reconstruction via K and π decay channels, one needs to carry out the K and π identification study before proceeding to calculate the quantities of D^0s. The identification of K and π hadrons is done by combining information from different detectors. First, the selected tracks should have high reconstruction efficiency. We require the transverse momentum (p_T) of the track larger than 0.6 GeV/c and pseudo-rapidity (η) within -1 and 1. In the anlysis, nHitsFit denotes the number of points which is used for fitting the track

and nHitsMax denotes the maximum number of points possible for that track. nHitsFit and nHitsFit/nHitsMax are required to ensure high tracking efficiency as well. Global distance of the closest approaches (gDCA) is a cut on the DCA of the track to the event vertex. By requiring the TPC tracks to be 1.5 cm away from the vertex ensures maximum efficiency. Once a cut on the DCA to vertex is placed, the track is refitted to include the vertex in the fit which increases the momentum resolution. The refitted tracks are called primary tracks. The hits on HFT are required to ensure good resolution of the track DCA. The track quality cuts implemented in this analysis are listed below:

- global tracks are required for the reconstruction of the secondary vertex;

- $p_T > 0.6$ GeV/c;

- rapidity range in $|\eta| < 1$;

- nHitsFit ≥ 20, in TPC;

- at least one hit in every layer of PXL and IST.

The particle identification (PID) is done using the ionization energy loss (dE/dx) in the TPC and the velocity (β) from the ToF detector. We require that $|n\sigma|$ is within less than 3 for π hadrons and within less than 2 for K hadrons. For tracks with available TOF information, a difference of $|\frac{1}{\beta} - \frac{1}{\beta_{exp}}|$ less than 0.03 is required for kaons and pions, respectively. The PID cuts are listed below:

- $|nSigmaPion| < 3.0$, based on TPC dE/dx;

- If pion TOF information is available: $|\frac{1}{\beta} - \frac{1}{\beta_{exp}}| < 0.03$;

- $|nSigmaKaon| < 2.0$, based on TPC dE/dx;

- If kaon TOF information is available: $|\frac{1}{\beta} - \frac{1}{\beta_{exp}}| < 0.03$

Table 3.1. Standard topological cuts used for Run 2014 data

D^0 p_T (GeV/c)	$0-1$	1-2	2-3	3-5	5-10
decay length (μm) >	145	181	212	247	259
DCA between 2 daughters (μm) <	84	66	57	50	60
DCA between D^0 and PV (μm) <	61	49	38	38	40
DCA between π and PV (μm) >	110	111	86	81	62
DCA between K and PV (μm) >	103	91	95	79	58
pointing angle ($\cos\theta$) >	0.99	0.99	0.99	0.99	0.99

3.3   Topological Cut Tuning with Toolkit for Multi-variable Analysis (TMVA)

The decay topological cuts are tuned in order to reduce the background and enhance the signal to background ratio. The topological cut variables are optimized using the Toolkit for Multivariate Data Analysis(TMVA) package. The details are discussed in the v_2-analysis note psn0651 [39].

For Run-2014 data analysis, the topological cuts are tuned for 6 different transverse momentum regions for all centrality classes. Table 3.1 shows the default topological cuts (tuned for $D^0 v_2$ analysis) used for D^0 v_1 analysis.

For the Run-2016 data, the topological cuts are further optimized in order to reduce background and enhance signal to background ratio. The topological cuts are tuned for 5 different centrality intervals and 6 different transverse momentum ranges, shown in Table 3.2.

Table 3.2. Standard topological cuts used for Run 2016 data

D^0 p_T (GeV/c)	$0 - 0.5$	0.5-1	1-2	2-3	3-5	5-10
Centrality 60-80%						
decay length (μm) >	150	107	175	187	164	175
DCA between 2 daughters (μm) <	73	88	92	82	83	104
DCA between D^0 and PV (μm) <	75	66	64	50	58	38
DCA between π and PV (μm) >	100	96	93	94	59	50
DCA between K and PV (μm) >	113	103	81	66	46	38
pointing angle cos (θ) >	0.95	0.95	0.95	0.95	0.95	0.95
Centrality 40-60%						
decay length (μm) >	140	133	190	201	215	219
DCA between 2 daughters (μm) <	76	87	90	82	101	93
DCA between D^0 and PV (μm) <	65	64	46	49	54	57
DCA between π and PV (μm) >	107	106	97	78	63	56
DCA between K and PV (μm) >	110	112	81	63	64	44
pointing angle cos (θ) >	0.95	0.95	0.95	0.95	0.95	0.95
Centrality 20-40%						
decay length (μm) >	149	170	205	236	234	237
DCA between 2 daughters (μm) <	78	67	69	66	73	99
DCA between D^0 and PV (μm) <	45	48	42	43	52	55
DCA between π and PV (μm) >	117	106	97	66	64	56
DCA between K and PV (μm) >	98	89	74	85	63	49
pointing angle cos (θ) >	0.95	0.95	0.95	0.95	0.95	0.95
Centrality 10-20%						
decay length (μm) >	151	173	204	240	237	231
DCA between 2 daughters (μm) <	70	70	62	67	76	85
DCA between D^0 and PV (μm) <	52	49	43	42	43	50
DCA between π and PV (μm) >	98	110	101	86	70	61
DCA between K and PV (μm) >	111	99	91	97	62	61
pointing angle cos (θ) >	0.95	0.95	0.95	0.95	0.95	0.95
Centrality 0-10%						
decay length (μm) >	128	163	222	214	241	253
DCA between 2 daughters (μm) <	66	79	61	63	76	68
DCA between D^0 and PV (μm) <	61	46	42	41	37	48
DCA between π and PV (μm) >	109	106	81	92	80	57
DCA between K and PV (μm) >	104	99	73	86	67	56
pointing angle cos (θ) >	0.95	0.95	0.95	0.95	0.95	0.95

3.4 D^0 **Signals**

Fig. 3.2 shows the invariant mass of $K\pi$ after topological cuts. The different panels are for different p_T bins. The red histograms are like-sign pair and blue histograms are mixed event to be explained later. The primary vertex used here is fit using the Kalman filter (KF) algorithm, with better vertex resolution than the default PV reconstruction [38]. There are some correlated background in the foreground, making it higher than the like-sign and mixed event background outside the D^0 peak region. They contribute to the "bump" at lower invariant mass region from other decay channels of D mesons and a shoulder below the D^0 peak from double mis-PID (K identified as π while π identified as K), which are described in later sub-sections. The invariant mass distributions are fit with a function of Gaussian distribution and a linear function. The parameter μ and σ from the Gaussian distribution present the peak position and the standard deviation, respectively. We define the candidates pairs as the unlike sign pairs with invariant mass in a range of -3σ to 3σ (the mass window). The side band is defined as invariant mass in a range of -9σ to -4σ and 4σ to 9σ.

3.5 **Efficiency and Acceptance Corrections**

Trigger Efficiency:

The VPD minbias trigger has a lower trigger efficiency for peripheral compared to central collisions. There is an additional weight to deal with different centrality distributions for different vertex z, due to VPD vertex z resolution for different centralities. These weights are taken care in "StRefMultCorr" class. We have used inverse of this trigger efficiency as weight while filling the D^0 v_1 histograms.

Reconstruction Efficiency:

The D^0 reconstruction efficiency comprises of:
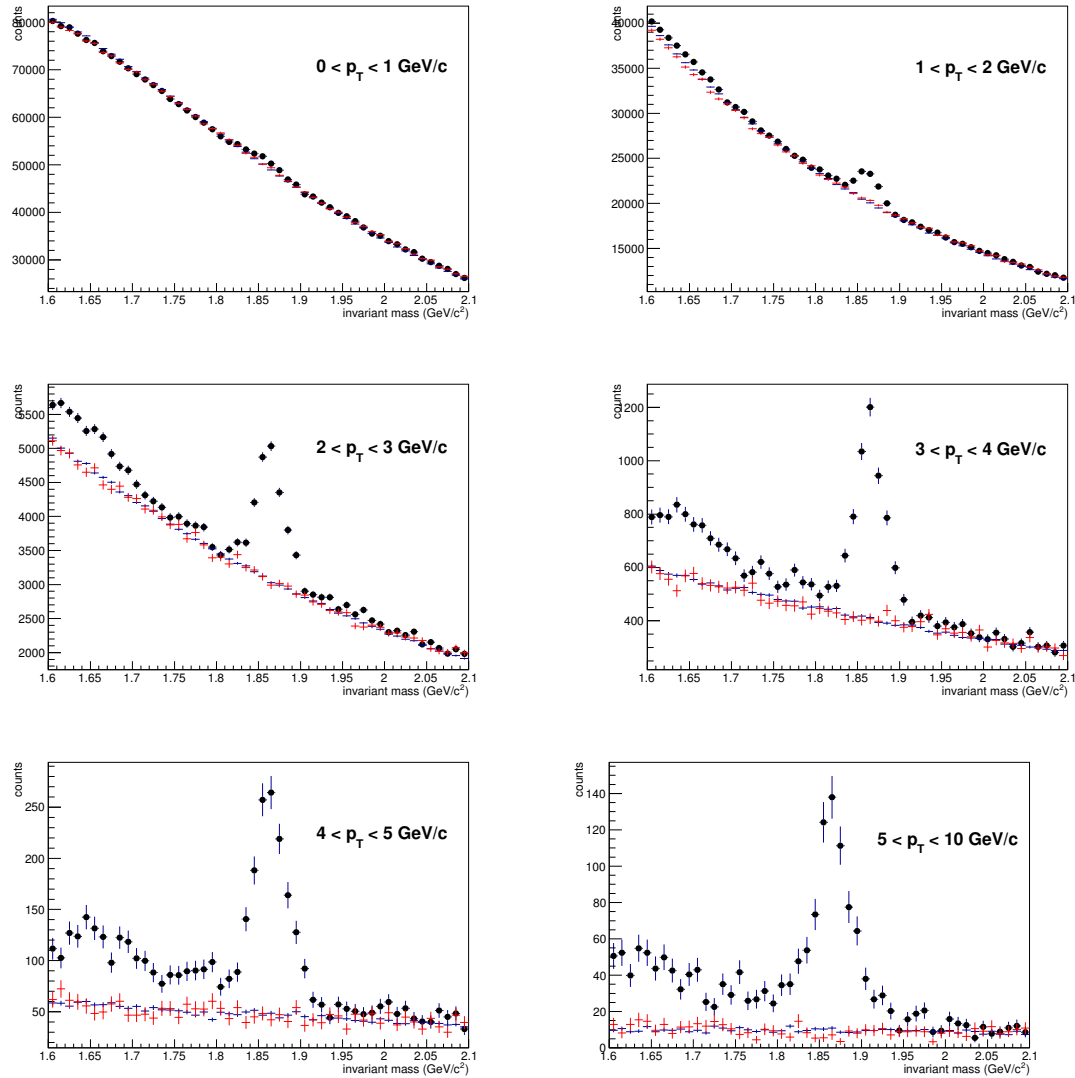
Figure 3.2. Example of invariant mass of $K\pi$ with D^0 signals in Run-14 after topological cut for different p_T bins. The red histograms are for like-sign pairs, the black histograms are for unlike-sign pairs, the blue histograms are for mixed event.

- TPC acceptance and efficiency (ϵ_{TPC}): The TPC acceptance and efficiency is obtained from standard STAR TPC embedding framework. The detail of TPC reconstruction efficiency is discussed in the D^0 spectra analysis note [40]

- HFT acceptance, tracking and topological cut efficiency (ϵ_{HFT}): The HFT related efficiency is calculated using a data driven simulation approach to best capture the HFT detector performance. This method has been described in detail in the D^0 spectra analysis note and the related paper draft [40].

- The efficiency related to particle identification (ϵ_{PID}) in TPC and TOF was also considered.

The D^0 reconstruction efficiency is thus: $\epsilon_{REC} = \epsilon_{TPC} \times \epsilon_{HFT} \times \epsilon_{PID}$.

The top panels of Fig. 3.3 present the reconstruction efficiency (ϵ_{REC}) as function of p_T in four different rapidity windows for D^0s and $\overline{D}^0$s in 0-80% central 200 GeV Au+Au collisions at RHIC run 2014 and 2016, respectively. The bottom panels show ratio of efficiency in negative and positive rapidity windows. The inverse of efficiency ($\epsilon_{REC}(\text{centrality}, p_T, \eta)$) is applied as a weight to the invariant mass histogram for the D^0 and $\overline{D}^0$.

Figure 3.4 shows the impact of reconstruction efficiency correction on the D^0 v_1 measurements, for 2014 data. The figure shows the D^0 and $\bar{D}^0$ v_1 results without and with efficiency corrections applied as a function of p_T, centrality and efficiency corrections applied as a function of p_T and η and centrality. The efficiency corrections do not change the v_1 appreciably, although the error bars get slightly increased as the lower p_T and forward rapidity regions with lower signal significance and lower efficiency get a higher weight.

Figure 3.5 shows the same comparison as Fig. 3.4 for the 2016 data. Again the central values do not change appreciably with the efficiency correction. In 2016, due to a dead sector in the HFT, a strong ϕ dependence to the acceptance was present. The efficiency
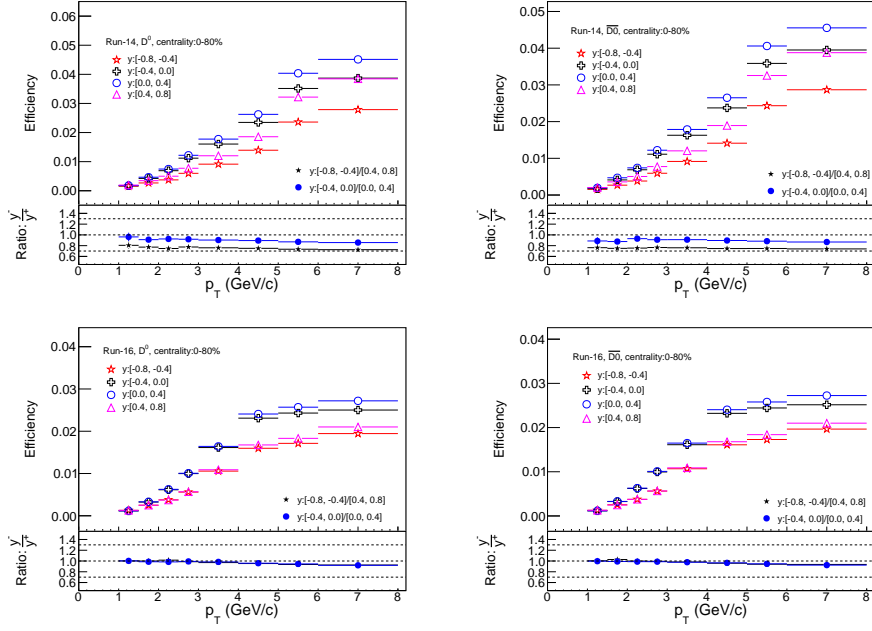
Figure 3.3. D^0 acceptance and efficiency as function of p_T in different rapidity windows for 0-80% central Au+Au collisions at 200 GeV. Top left panel: efficiency for D^0 mesons in Run-2014, top right panel: efficiency for $\overline{D}^0$ in Run-2016(production-1), bottom left panel: efficiency for D^0 mesons in Run-2016, and bottom right panel: efficiency for $\overline{D}^0$ mesons in Run-2016(production-1)
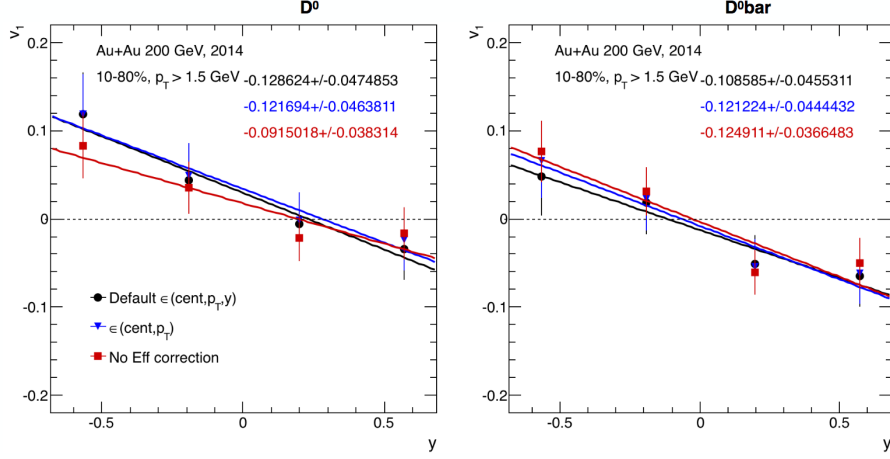
Figure 3.4. D^0 (left) and $\bar{D}^0$ (right) v_1 from 2014 data, without efficiency correction, with p_T and centrality dependent efficiency correction and p_T, centrality and η dependent efficiency correction.

correction was also applied as a function of p_T, ϕ and centrality. To check for potential impact from this, the results with ϕ dependent efficiency corrections are shown in Figure 3.6. As in the previous cases, the values change only moderately.

As we have seen, the v_1 results with efficiency weights have moderate impact on the data but it enhances the statistical uncertainties of the data points. We keep the results without the efficiency weight as default, and consider the difference with efficiency weights as a source of systematic uncertainty.
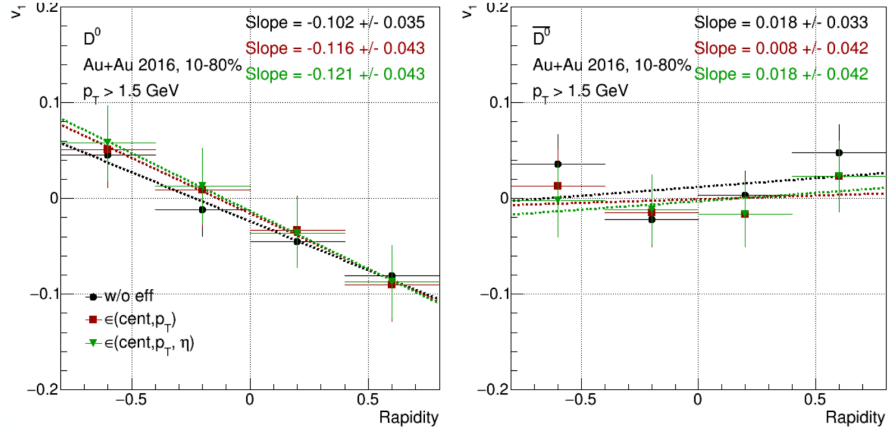
Figure 3.5. D^0 (left) and $\bar{D}^0$ (right) v_1 from 2016 data, without efficiency correction, with p_T and centrality dependent efficiency correction and p_T, centrality and η dependent efficiency correction.
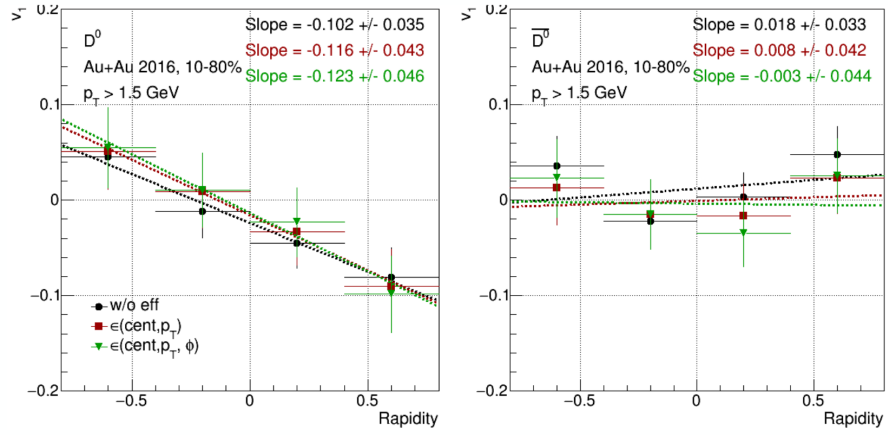
Figure 3.6. D^0 (left) and $\bar{D}^0$ (right) v_1 values from 2016 data, without efficiency correction, with p_T and centrality dependent efficiency correction and p_T, centrality and ϕ dependent efficiency correction.

4. D^0 DIRECTED FLOW (V_1)

4.1 Event Plane Method

4.1.1 ZDC Event Plane Reconstruction

In this thesis, the first order event plane is reconstructed using the ZDC-SMD detectors located on both east and west side of the STAR detector at $|\eta| > 6.4$. In this method we utilize the sideward deflection of spectator neutrons measured in the ZDC-SMD. The ZDC-SMD is made of 7 vertical slats and 8 horizontal slats. The two SMDs provide event-by-event information on the transverse distribution of energy deposition of the spectator neutrons. The weighted center of the energy distribution determines the event plane vector on each side. The combination of the east and west event plane vectors provides the full event plane. Measurements using ZDC-SMD are sensitive to the calibration. Since the transverse position of the beam is not stable, the centroid in ZDC-SMD varies from time to time. This beam center calibration is done, before reconstructing the event plane. In addition the ADC distributions are pedestal subtracted and gain corrected in order to make a uniform gain over all the detector slats. The pedestal subtraction is automatic after February 2011. To make the response of the detector uniform, we need to adjust the gain parameters in different ZDC-SMD channels. We have followed the method prescribed in Reference [41] for gain calibration. First, we fit the ADC distribution for each horizontal/vertical and east/west slats of ZDC-SMD with an exponential function $Ae^{(-B \times ADC)}$. If the response of the detector is uniform, then the high-ADC tail should have the same behavior for all the channels. Then after the exponential fitting, the parameter B for each horizontal/vertical and east/west slats of ZDC-SMD is used to obtain the gain correction factors. The flow vectors Q_n are constructed as

$$Q_{1,x} = \sum_{i=1}^{i=7} w_i x_i \qquad (4.1)$$

$$Q_{1,y} = \sum_{i=1}^{i=8} w_i y_i, \tag{4.2}$$

where x_i and y_i are the fixed position for the 7 vertical slats and 8 horizontal slats in the ZDC-SMD. The weights are given by

$$w_i = \frac{ADC_i}{\sum_i^{7,or8} ADC_i} \tag{4.3}$$

As mentioned above, the ZDC-SMD centroid is not stable, so we need to apply beam center correction [41]. First, we store the average x,y position ($\langle x \rangle$, $\langle y \rangle$) of the cluster for each east/west ZDC-SMD as a function of run-index. Then the averages of $\langle x \rangle$ and $\langle y \rangle$ values are used to correct the x and y positions as function of run-index. After gain calibration and beam centering, the Q-vectors are reconstructed using Eq. 4.1 and Eq. 4.2. Then the first order event plane is reconstructed as:

$$\Psi_1 = arctan[\frac{\sum_{i=1}^{i=7} w_i x_i}{\sum_{i=1}^{i=8} w_i y_i}] \tag{4.4}$$

Event plane should be randomly distributed, but because of the rectangular geometry of the ZDC-SMD the shape of the event plane distribution is not flat even if it is weighted by ADC. To make it flat, a further shifting method is applied. It makes the correction to the event plane itself, to get the flat event plane distribution. The shift correction for n^{th} harmonic event plane is

$$\Delta\Psi_n = \frac{1}{n} \sum_i^{i_{max}} \frac{2}{i}[-\langle\sin(in\Psi_n)\rangle \cos(in\Psi_n) + \langle\cos(in\Psi_n)\rangle \sin(in\Psi_n)], \tag{4.5}$$

where gives The final corrected event plane angle as

$$\Psi_n' = \Psi_n + \Delta\Psi_n \tag{4.6}$$

The shift corrections are usually done in 10% centrality bins. However, if there is a centrality dependence for the shift correction, even after rendering the Ψ_1 distribution isotropic

in 10% centrality bins, residual correlations with detector effects can show up in the v_n measurements. To remedy this, our shift corrections are changed to make the Ψ_1 distributions isotropic in 2% centrality bins. The distribution of ZDC-SMD event planes from "st-physics", "st-sst" and "st-nosst" streams before and after flattening are shown in Fig 4.1. Due to the finite multiplicity of events, the event plane angle Ψ_1 may not coincide with the reaction plane angle Ψ_R. Hence, a resolution correction need to be performed to obtain the correct measurement of the flow coefficient. For the case of the first-order event plane from the ZDC, the event plane resolution for the k-th harmonic is $\langle \cos k[(\Psi_1 - \Psi_R)] \rangle$. The ZDC event plane obtained from the detector on each side of the collision (east or west) is called a sub-event plane. We have two independent sub-event planes from the two ZDCs. The correlation between these two event plane angles can be expressed as,

$$\langle \cos k[(\Psi_{east} - \Psi_{west})] \rangle = \langle \cos k[(\Psi_{east} - \Psi_R)] \rangle \langle \cos k[(\Psi_{west} - \Psi_R)] \rangle \tag{4.7}$$

If we assume that the two sub-event planes have the same resolution, then the sub-event plane resolution is

$$\langle \cos k[(\Psi_{sub} - \Psi_R)] \rangle = \langle \cos k[(\Psi_{east} - \Psi_R)] \rangle = \langle \cos k[(\Psi_{west} - \Psi_R)] \rangle = \sqrt{\langle \cos k[(\Psi_{east} - \Psi_{west})] \rangle} \tag{4.8}$$

A combination of the east and west sub-event plane vectors provides the full event plane. When the sub-event plane resolution is low, we can approximate the full event plane resolution as

$$\langle \cos k[(\Psi_{full} - \Psi_R)] \rangle = \sqrt{2} \langle \cos k[(\Psi_{sub} - \Psi_R)] \rangle, \tag{4.9}$$

which can be obtained from the sub-event plane resolution. A more accurate estimation of the event plane resolution (from Ref. [24]) used in this analysis is given by

$$\langle \cos km[(\Psi_m - \Psi_R)] \rangle = \frac{\sqrt{\pi}}{2\sqrt{2}} \chi_m exp(-\chi_m^2/4)[I_{(k-1)/2}(\chi_m^2/4) + I_{(k+1)/2}(\chi_m^2/4)], \tag{4.10}$$

where $\chi_m = v_m/\sigma$ and I_ν is the modified Bessel function of order ν. The χ_m can be obtained from the sub-event plane resolution as shown in Fig. 1 of Ref. [24]. Figure 4.2 presents the first order event plane resolution as function of centrality calculated from the correlation between east and west side of ZDC-SMD. The open circle and star symbols present the results from RHIC runs during the year 2014 and 2016, respectively. The resolutions are compared to Run 2011 results. We find that the ZDC-SMD first order event plane resolution is consistent among RHIC runs in different years.
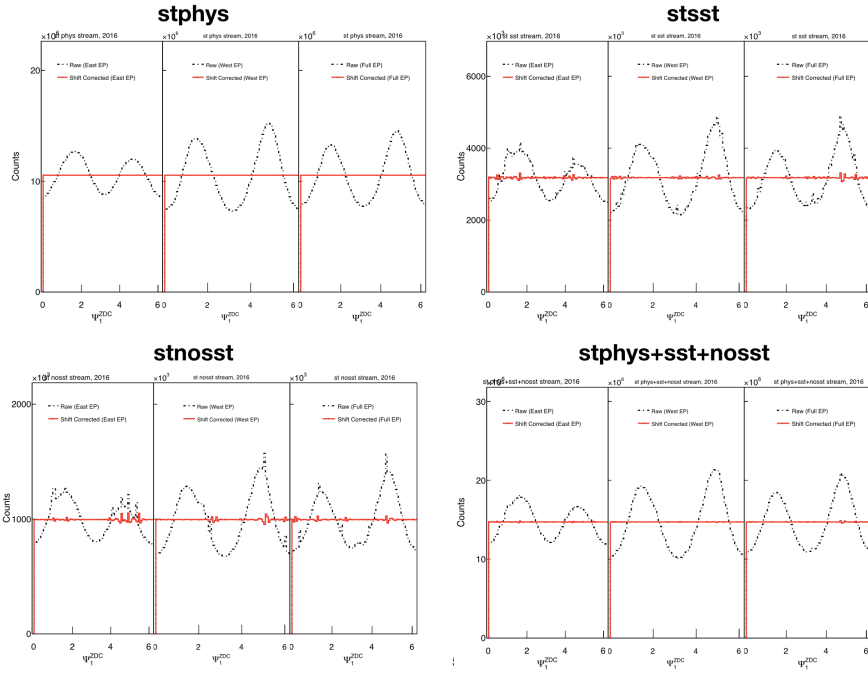
Figure 4.1. First order event plane distribution from Run 2014 and Run-2016

4.1.2 Directed Flow Calculation

The directed flow is calculated using the standard event-plane method. The D^0 yields are measured in azimuthal bins relative to the event-plane azimuth $\phi - \Psi$. The observed v_1^{obs} is then calculated by fitting the D^0-yield with a functional form $p_0[1 + v_1^{obs}\cos(\phi - \Psi)]$. Figure 4.3 presents the D^0-yield as function of $\phi - \Psi_1$ for $p_T > 1.5$ GeV/c and $-0.8 <$
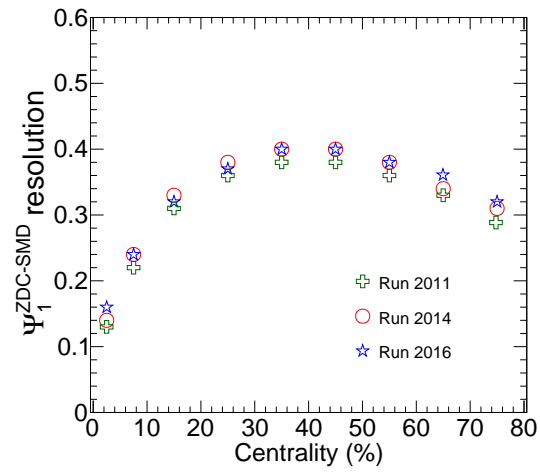
Figure 4.2. First order event plane resolution as a function of collision centrality in Au+Au collisions at 200 GeV. Solid red circle and open blue star markers present results from RHIC run 2014 and 2016, respectively. Results are compared to Run-11 results shown by green plus symbols.

$y < 0.8$ in 10-80% central Au+Au collisions. The resolution-corrected v_1 is then obtained by dividing v_1^{obs} by the Ψ_1 event-plane resolution. The event plane resolution for wide centrality bins (here 10-80%) are obtained by the D^0-yield-weighted average of event plane resolution.
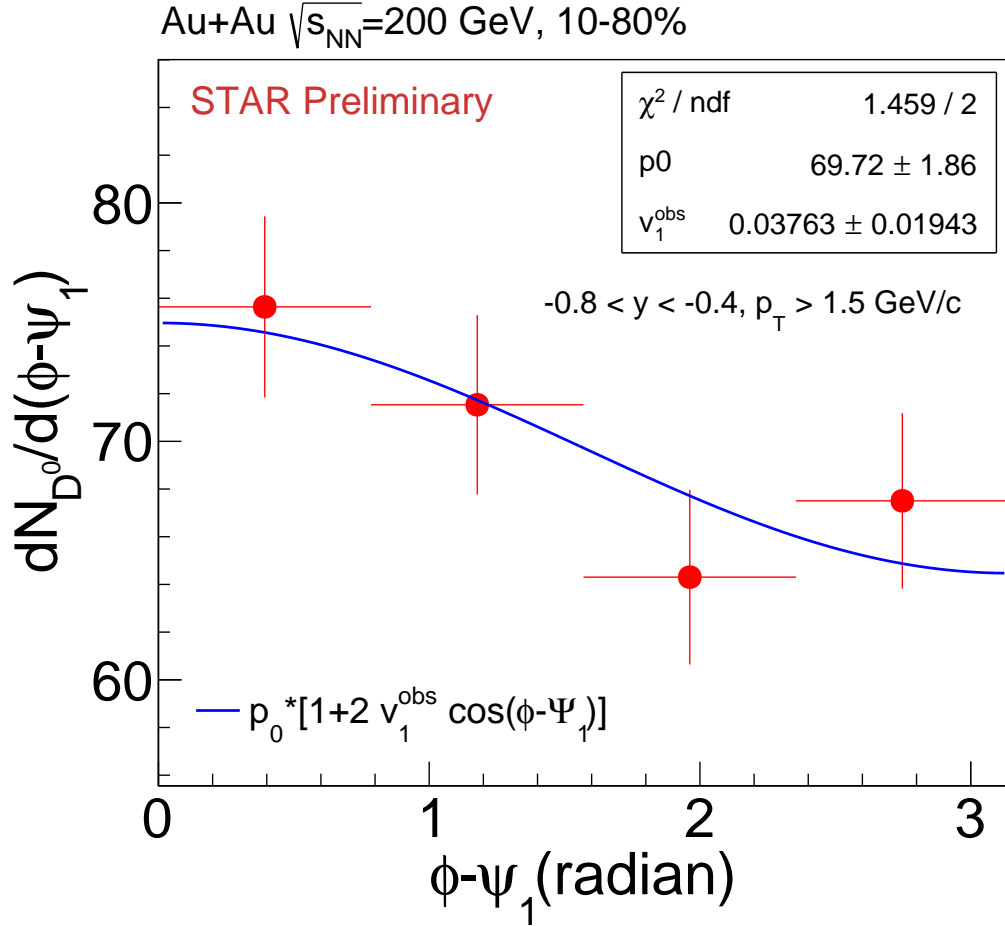
Figure 4.3. An example of fitting D^0 yield as a function of $\phi - \psi_1$ for $p_T(D^0) > 1.5$ GeV/c within $-0.8 < y < -0.4$.

For the run 2014 analysis, we have used the "stphys" stream data, while for run 2016 we used the "stphys" stream from the production-1 and the "stsst" and the "stnosst" from production-2. Figure 4.4 shows the comparison of D^0 (top-panel) and $\overline{D^0}$ (right-panel)
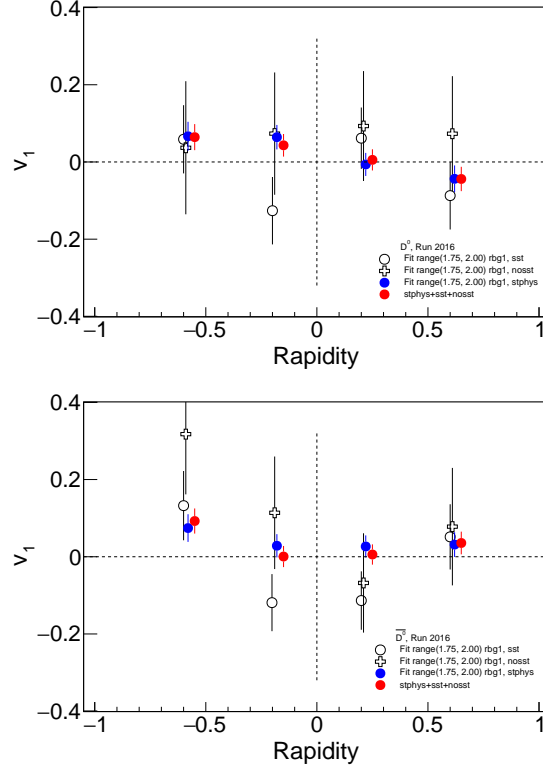
Figure 4.4. D^0 and $\overline{D^0}$ v_1 vs rapidity from Run 2016 streams: stphys, stsst and stnosst.

from three different streams in run 2016. For 2016 results, we have merged the invariant mass versus $\phi - \Psi$ histograms from "stphys", "stsst" and "stnosst" and calculated the v_1.

The top panel in Fig 4.5 shows the comparison of $v_1(y)$ from run 2014 (stphys) and 2016 (stphys+stsst+stnosst) represented by open black and blue markers. The results from run 2014 and 2016 are combined with the inverse of statistical errors as a weight shown by solid red circles. The v_1 slopes from 2014, 2016, and combined 2014+2016 data are also reported. The same is presented for $\overline{D^0}$ in the bottom panel of Fig 4.5. Table 4.1 presents the comparison of v_1 and statistical significance (σ) of the difference between run 2014 and 2016 results. One can see that D^0 points from run 2014 and 2016 are consistent within 1σ level. For the $\overline{D^0}$, first two rapidity bins consistent within 1σ level while the last two points are at 1.27 and 1.74σ. The combined D^0 and $\overline{D^0}$ data points are consistent within maximum 1.4σ.
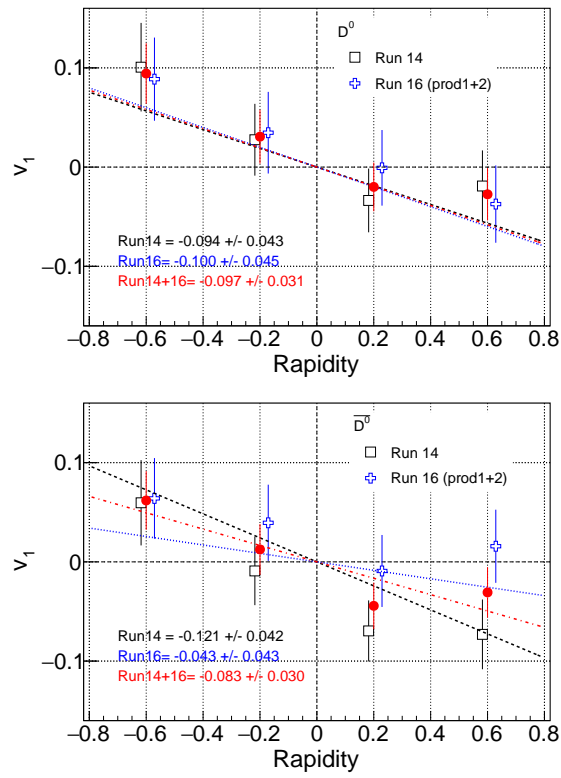
Figure 4.5. Comparison of D^0 and $\overline{D^0}$ $v_1(y)$ from run 2014 and run 2016 data.

Table 4.1. Comparison of D^0 and $\overline{D^0}$ $v_1(y)$ from run 2014 and 2016 and their statistical significance (σ) difference

D^0 rapidity	$[-0.8, -0.4]$	$[-0.4, 0.0]$	$[0.0, 0.4]$	$[0.4, 0.8]$
Run 2014	0.1007 ± 0.0446	0.0276 ± 0.0362	0.0336 ± 0.0321	0.0190746 ± 0.0359
Run 2016	0.0886 ± 0.0419	0.0347 ± 0.0411	-0.0007 ± 0.0381	-0.0373 ± 0.0390
σ of diff	0.1970	0.1295	0.6599	0.3439
$\overline{D^0}$ rapidity	$[-0.8, -0.4]$	$[-0.4, 0.0]$	$[0.0, 0.4]$	$[0.4, 0.8]$
Run 2014	0.0596 ± 0.0430	0.0091 ± 0.0345	-0.0696 ± 0.0307	-0.0731 ± 0.0351
Run 2016	0.0640 ± 0.0406	0.0394 ± 0.0384	-0.0092 ± 0.0362	0.0157 ± 0.0369
σ of diff	0.0748	0.9350	1.2702	1.7439
$D^0 + \overline{D^0}$ rapidity	$[-0.8, -0.4]$	$[-0.4, 0.0]$	$[0.0, 0.4]$	$[0.4, 0.8]$
Run 2014	0.0794 ± 0.0309	0.0083 ± 0.0250	-0.0524 ± 0.0222	-0.04663 ± 0.0251
Run 2016	0.0759 ± 0.0292	0.0372 ± 0.0281	-0.0052 ± 0.0263	-0.0093 ± 0.0268
σ of diff	0.0805	0.7674	1.3725	1.0168

4.2 Systematic Uncertainties

Systematic uncertainties are calculated by comparing the v_1 obtained from the following different methods:

- the fit (default) vs. side-band methods (shown in Fig 4.6). For the fit method the yield is extracted by subtracting the linear residual background function underneth signal within the range 1.75-2.00 GeV/c^2. For the side-band method, the signal region window is the same as above, while the background regions in the left and right side are chosen as 1.71-1.80 GeV/c^2 and 1.93-2.02 GeV/c^2.

- by varying invariant mass fitting ranges and background functions: first-order (default) vs. second-order polynomial, or exponential, or power-law functions (shown in Figs. 4.7 and 4.8). In the default settings, the fitting range of 1.75-2.00 GeV/c^2 and linear residual backgrounds are considered. The impact on the results from directly fitting the unlike-sign yields to a Gaussian+background function and from fitting after subtraction of the background of unlike-sign pairs from mixed-event background is also studied.

- yield extraction methods: histogram bin counting (default) vs. functional integration (shown in Fig. 4.9).

- varying topology cuts so that the efficiency changes by 50% with respect to nominal value (shown in Fig. 4.10). The maximum difference between the default and tighter topology cuts may be an over-estimation because the statistical uncertainties also contribute to the difference. The uncorrelated statistical uncertainties can be evaluated as follows. Consider the default measurement to be $(d + \sigma_d)$ and an alternative tighter cut to be $(t \pm \sigma_t)$. Then, $\Delta = t - d$ and $\sigma_\Delta^2 = \sigma_t^2 + \sigma_d^2 - 2\rho\sigma_t\sigma_d$, where ρ is the correlation coefficient, which is 0.84 for default and tighter cut. The difference between the rms of Δ and σ_Δ^2 is considered as the systematic due to topological cut variations.

- vertex Z cut variation: $|V_z| < 6$ (default) and 4 cm (shown in Fig. 4.11).
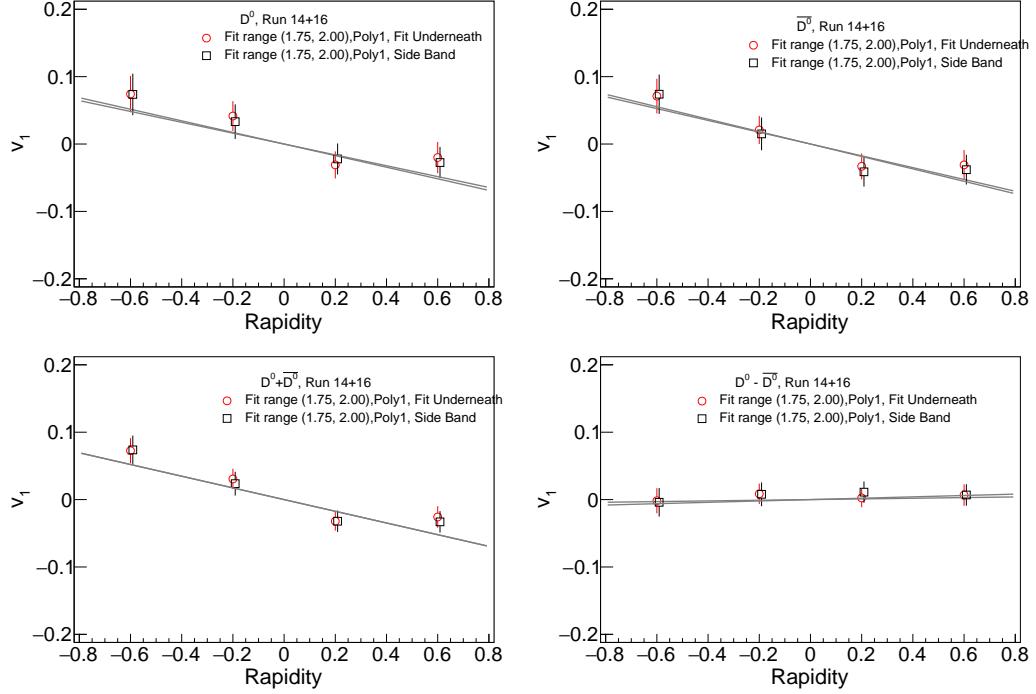
Figure 4.6. Systematic study for the $v_1(y)$ and dv_1/dy of D^0, $\overline{D^0}$, their average and difference due to fit function method and side band from Run 2014 and 2016 data.

- TOF $1/\beta$ cut variation: $1/\beta < 0.03$ (default) and 0.025 (shown in Fig. 4.11).

- With and without efficiency weights (shown in Fig. 4.12).

The above variations are done independently for the $v_1(y)$ and dv_1/dy of D^0s, $\overline{D^0}$s, their average ($D^0+\overline{D^0}$) and difference (D^0-$\overline{D^0}$). These variations in $v_1(y)$ and dv_1/dy are shown in Figs. 4.6, 4.7, 4.8, 4.9, 4.10, 4.11 and 4.12. For the final systematic uncertainty the maximum difference between the default and alternative measurements from the sources signal/yield extraction, all event/pid cut variations, with/without efficiency weights and the difference between default/tight topology cuts are added in quadrature. Furthermore, the systematic uncertainties between D^0 and $\overline{D^0}$ are smoothened out by symmetrizing in rapidity bins. The maximum systematic uncertainty is considered for symmetrization. The systematic related to the ZDC-SMD event plane resolution due to variation in calibration has been studied and found to be of the order of 1%.

Figure 4.7. Systematic study for the $v_1(y)$ and dv_1/dy of D^0, $\overline{D^0}$, their average and difference due to invariant mass fit range variations from Run 2014 and 2016 data.

Table 4.2. Systematic uncertainties for D^0 $v_1(y)$

$D^0 v_1(y)$	$[-0.8, -0.4]$	[-0.4,0.0]	[0.0,0.4]	[0.4,0.8]	v_1 slope
signal extraction	0.0090	0.0070	0.0077	0.055	0.0081
yield extraction	0.0030	0.0027	0.0020	0.0054	0.0052
event, pid cuts	0.009	0.009	0.0036	0.0009	0.058
topol. cuts	0.011	0.005	0.005	0.011	0.010
with/without efficiency weights	0.0091	0.0021	0.0022	0.0090	0.0082
total systematic error	0.0193	0.0129	0.0103	0.0185	0.01821

Figure 4.8. Systematic study for the $v_1(y)$ and dv_1/dy of D^0, $\overline{D^0}$, their average and difference due to residual fit function variations from Run 2014 and 2016 data.

Table 4.3. Systematic uncertainties for $\overline{D^0}$ $v_1(y)$

| $\overline{D^0}$ $v_1(y)$	$[-0.8, -0.4]$	[-0.4,0.0]	[0.0,0.4]	[0.4,0.8]	v_1 slope
signal extraction	0.011	0.0042	0.0060	0.0035	0.0077
yield extraction	0.0070	0.0060	0.0070	0.0071	0.0031
event, pid cuts	0.0073	0.0083	0.0042	0.00081	0.0076
topol. cuts	0.011	0.005	0.009	0.013	0.011
with/without efficiency weights	0.0092	0.009	0.009	0.013	0.013
total syst error	0.2071	0.01511	0.01626	0.0222	0.02041

Figure 4.9. Systematic study for the $v_1(y)$ and dv_1/dy of D^0, $\overline{D^0}$, their average and difference due to yield extraction by histogram bin counting vs function integration from Run 2014 and 2016 data.

Table 4.4. Systematic uncertainties for combined $D^0 + \overline{D^0}$ $v_1(y)$

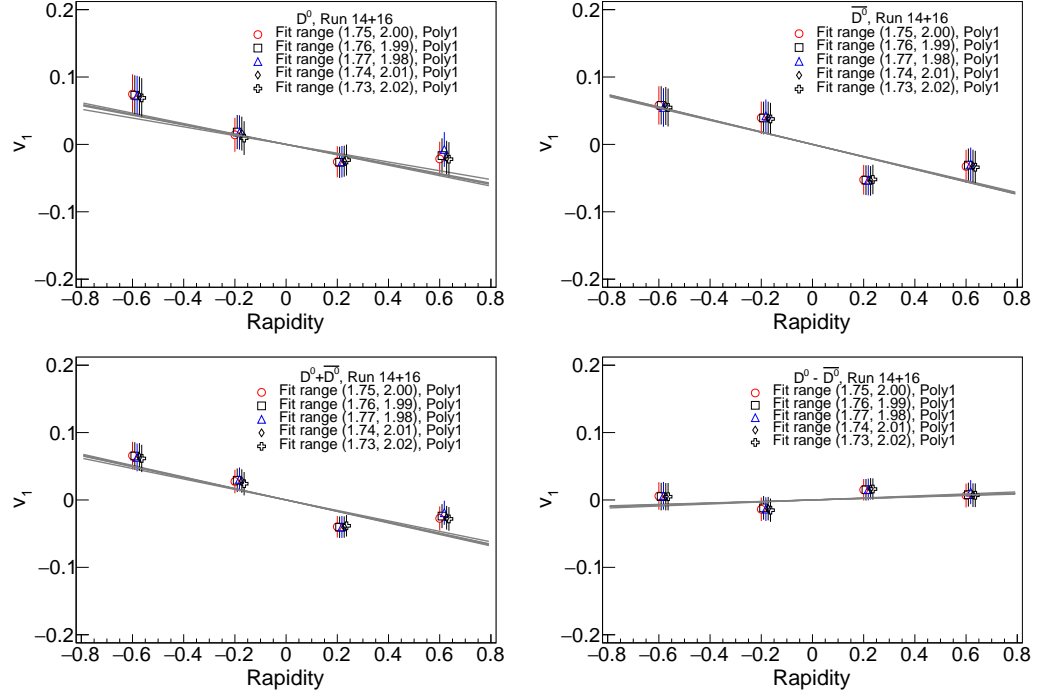| $D^0+\overline{D^0}$ $v_1(y)$	$[-0.8, -0.4]$	[-0.4,0.0]	[0.0,0.4]	[0.4,0.8]	v_1 slope
signal extraction	0.010	0.0032	0.0030	0.0085	0.0076
yield extraction	0.0027	0.0024	0.0031	0.0071	0.0041
event, pid cuts	0.0047	0.0065	0.0023	0.00041	0.0038
topol. cuts	0.014	0.0051	0.0051	0.0085	0.0085
with/without efficiency weights	0.0072	0.0073	0.0073	0.070	0.011
total syst error	0.2071	0.01511	0.01626	0.0222	0.011
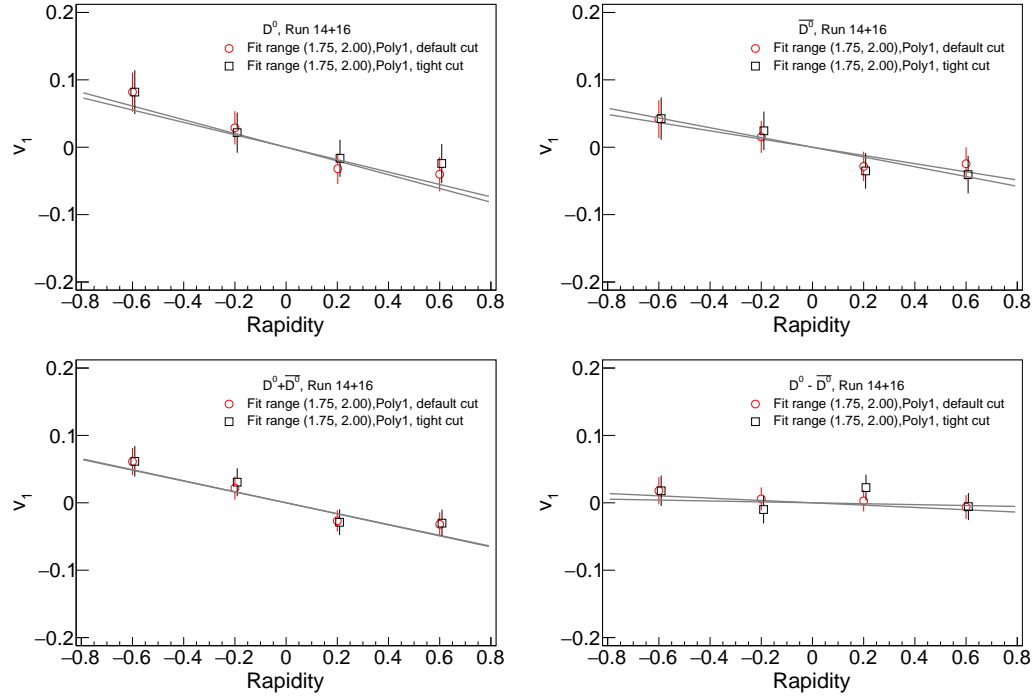
Figure 4.10. Systematic study for the $v_1(y)$ and dv_1/dy of D^0, $\overline{D^0}$, their average and difference due to topology cut variations (standard vs tight) from Run 2014 and 2016 data.

Table 4.5. Systematic uncertainties for combined D^0 - $\overline{D^0}$ $v_1(y)$

D^0 - $\overline{D^0}$ $v_1(y)$	$[-0.8, -0.4]$	[-0.4,0.0]	[0.0,0.4]	[0.4,0.8]	v_1 slope
signal extraction	0.0061	0.0032	0.0070	0.0051	0.0041
yield extraction	0.0057	0.0046	0.0046	0.0059	0.0051
event, pid cuts	0.0028	0.0047	0.0032	0.0085	0.0039
topol. cuts	0.011	0.0059	0.0083	0.011	0.0085
with/without efficiency weights	0.011	0.0093	0.0093	0.0088	0.045
total syst error	0.180	0.01296	0.01517	0.01817	0.0107
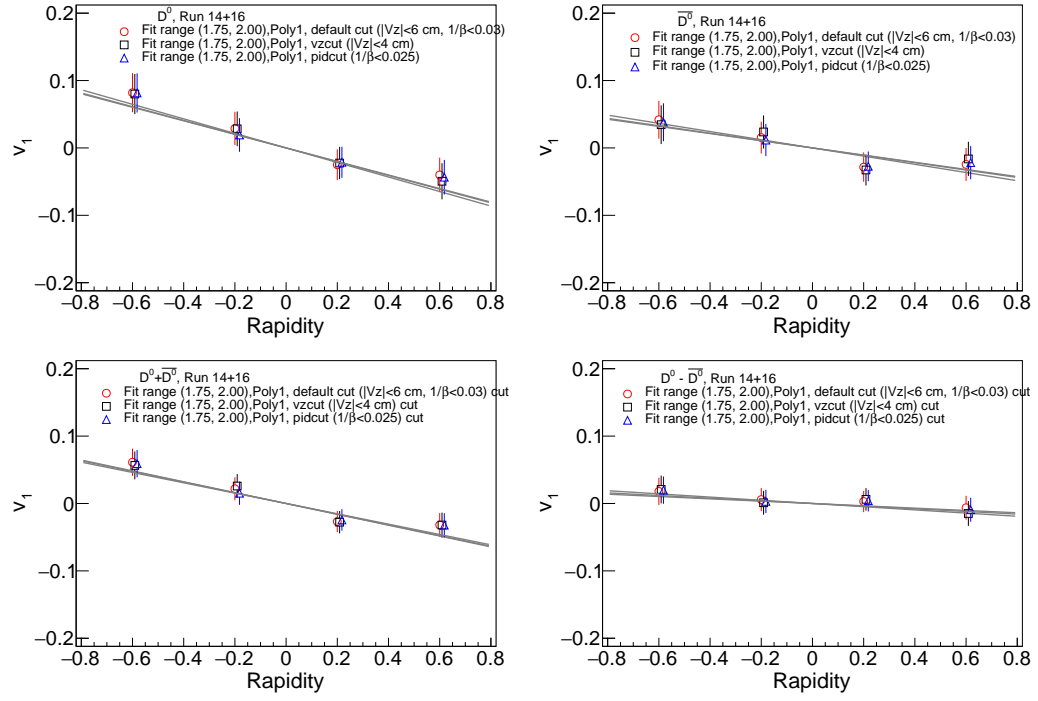
Figure 4.11. Systematic study for the $v_1(y)$ and dv_1/dy of D^0, $\overline{D^0}$, their average and difference due to event (TPC V_z cut) and PID (ToF $1/\beta$ cut) cut variations from Run 2014 and 2016 data.
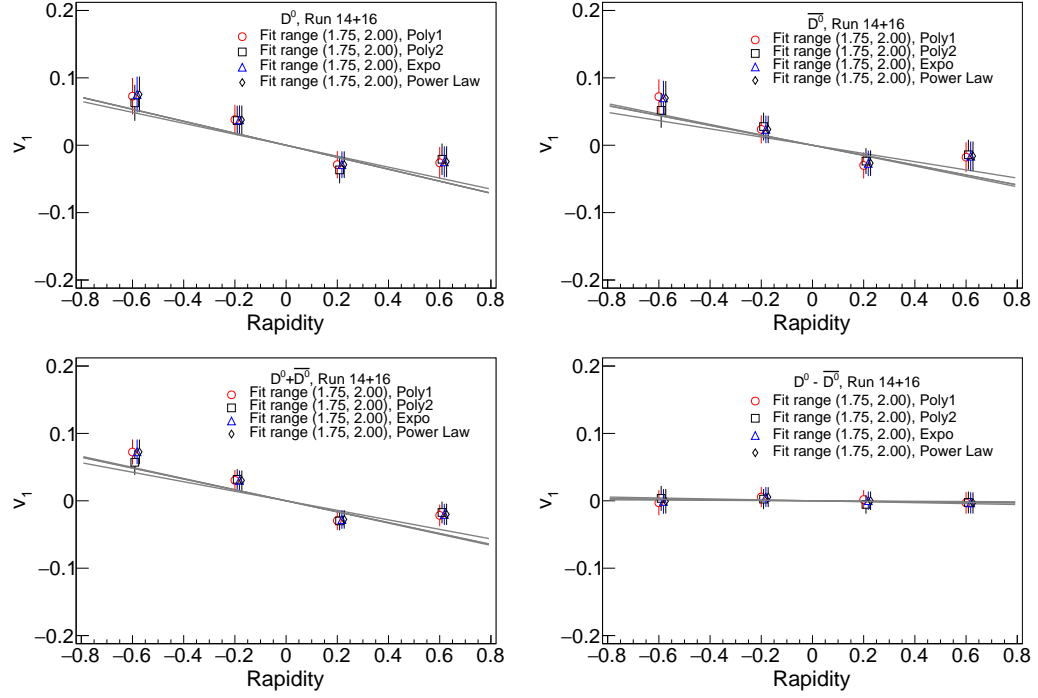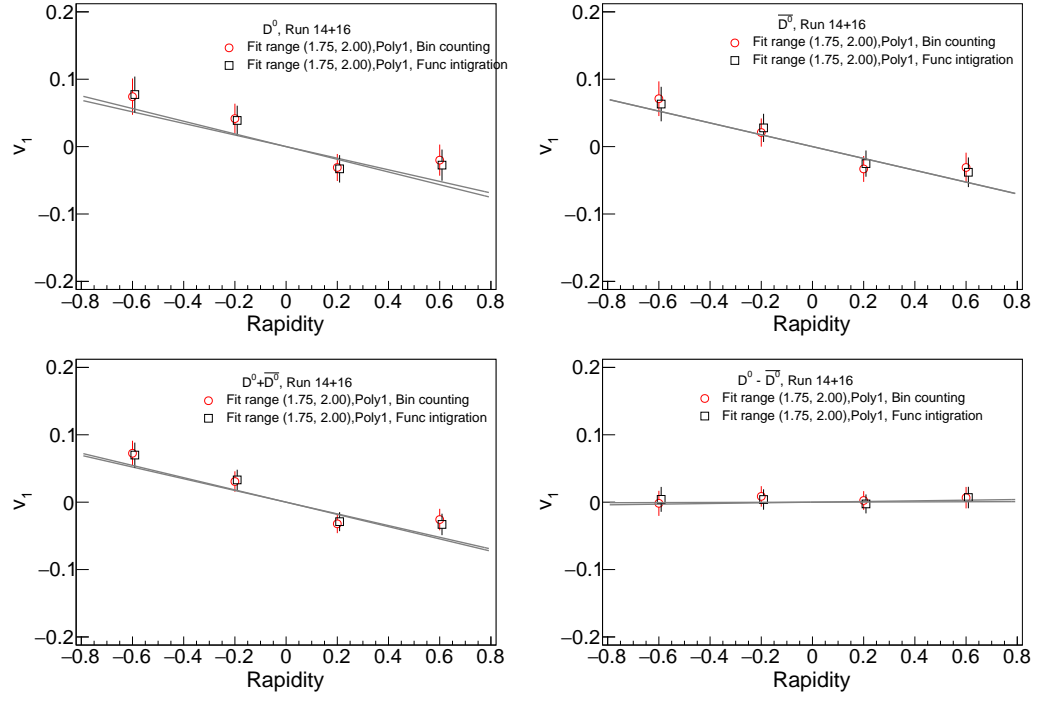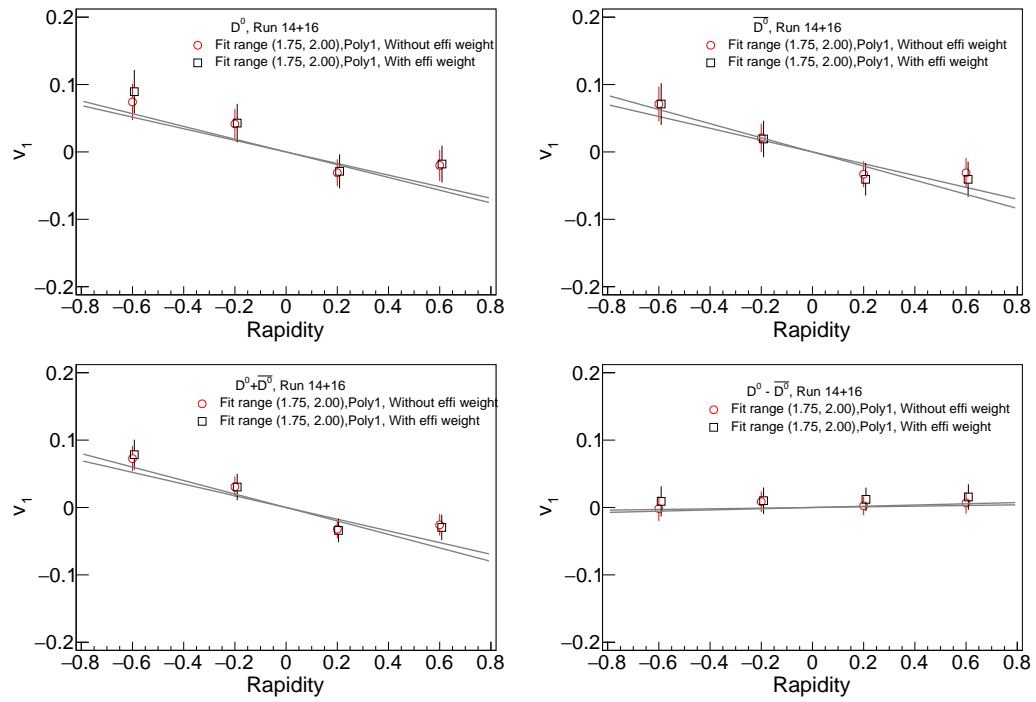
Figure 4.12. Systematic study for the $v_1(y)$ and dv_1/dy of D^0, $\overline{D^0}$, their average and difference due to efficiency weights (with and without efficiency weights) from Run 2014 and 2016 data.
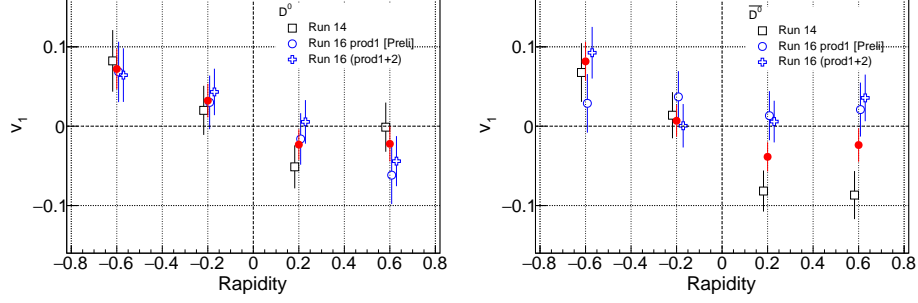
Figure 4.13. D^0 and $\overline{D^0}$ $v_1(y)$ from Run 2014 and 2016 (production1+production2) and their combination.

4.3   Results and Discussion

The D^0 v_1 from Run 2014 and Run 2016 results are combined with weight of the inverse of squared statistical uncertainty as shown in Figure 4.13.

Figure 4.14 presents the final results of individual D^0 and $\bar{D}^0$ $v_1(y)$ for 10-80% central Au+Au collisions, denoted by open circles and open star markers, respectively. The solid circles are for the average of D^0 and $\bar{D}^0$. The v_1 results are compared with K mesons shown by open square markers. The $v_1(y)$-slope for D^0 mesons is extracted by fitting the data with a linear function passing through the origin. The choice of linear function is driven by the limited D^0 statistics. The observed dv_1/dy for D^0 and $\bar{D}^0$ are $-0.102 \pm$ 0.030 (stat.) $\pm$ 0.021 (syst.) and -0.061 ± 0.030 (stat.) $\pm$ 0.023 (syst.), respectively, while dv_1/dy for their average is -0.081 ± 0.021 (stat.) ± 0.017 (syst.). The heavy flavor results are compared to the average of K^+ and K^- [42]. The kaon v_1 slope is based on a similar linear fit, and the fitted dv_1/dy for kaons is -0.0030 ± 0.0001 (stat.) ± 0.0002 (syst.). The D^0 dv_1/dy is about 20 times larger (2.9σ significance) than the kaon dv_1/dy, but the sign of dv_1/dy is the same for both.

Figure 4.15 presents the D^0 v_1 compared to a hydrodynamic model. The model calculation, combining the Langevin dynamics for the heavy quarks within the hydrodynamical background from the tilt bulk together with the initial electromagnetic field [28], predicts the correct sign of dv_1/dy for both D^0 and $\bar{D}^0$, but underestimates the magnitude with the
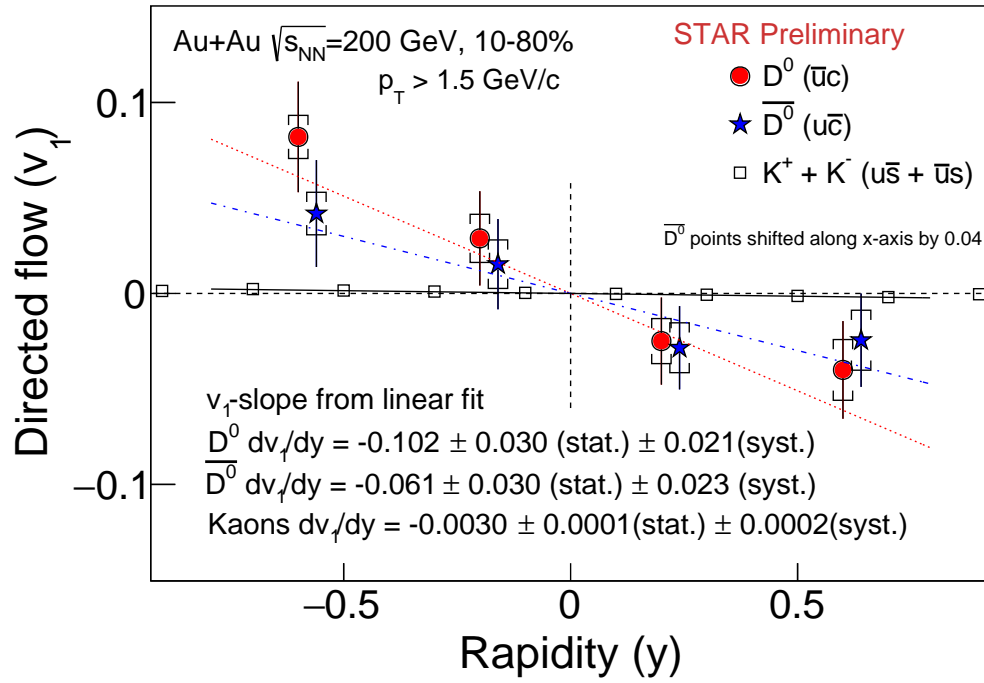
Figure 4.14. Red circles and blue stars represent D^0 and $\bar{D}^0$ v_1 as a function of rapidity for $p_T > 1.5$ GeV/c in 10-80% central Au+Au collisions at $\sqrt{s_{NN}} = 200$ GeV. The open squares represent the average v_1 for charged kaons. The D^0 and $\bar{D}^0$ v_1 are fit with a linear function and plotted as red and blue lines.
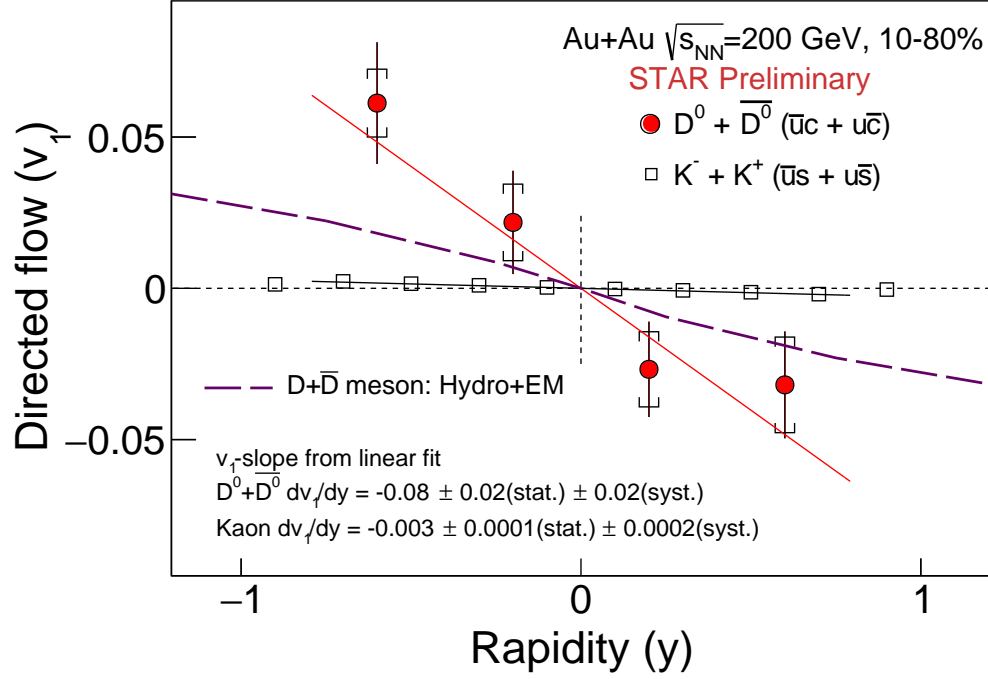
Figure 4.15. The red circles represent the average v_1 for combined D^0 and $\bar{D}^0$ for p_T > 1.5 GeV/c in 10-80% Au+Au collisions at $\sqrt{s_{NN}}$ = 200 GeV. The open squares are for average v_1 of charged kaons. The magenta dashed line is a hydrodynamic model calculation combined with the initial electromagnetic field.

choice of the used model parameters. Our results can therefore help constrain the model parameters, such as the tilt and the charm quark drag coefficient.

Figure 4.16 shows the comparison of the measured difference in v_1 (Δv_1) between D^0s and $\bar{D}^0$s to the theoretical predictions. The dashed magenta line is the calculation from a same model incorporating both the tilted bulk and the initial electromagnetic field [28]. The solid blue line is from the initial electromagnetic field only [29]. The measured Δv_1-slope is -0.041 ± 0.041(stat.)± 0.020(syst.), which is consistent with zero as well as with model calculations. The current precision of the data is not sufficient to draw conclusions regarding the effect of electromagnetic field.
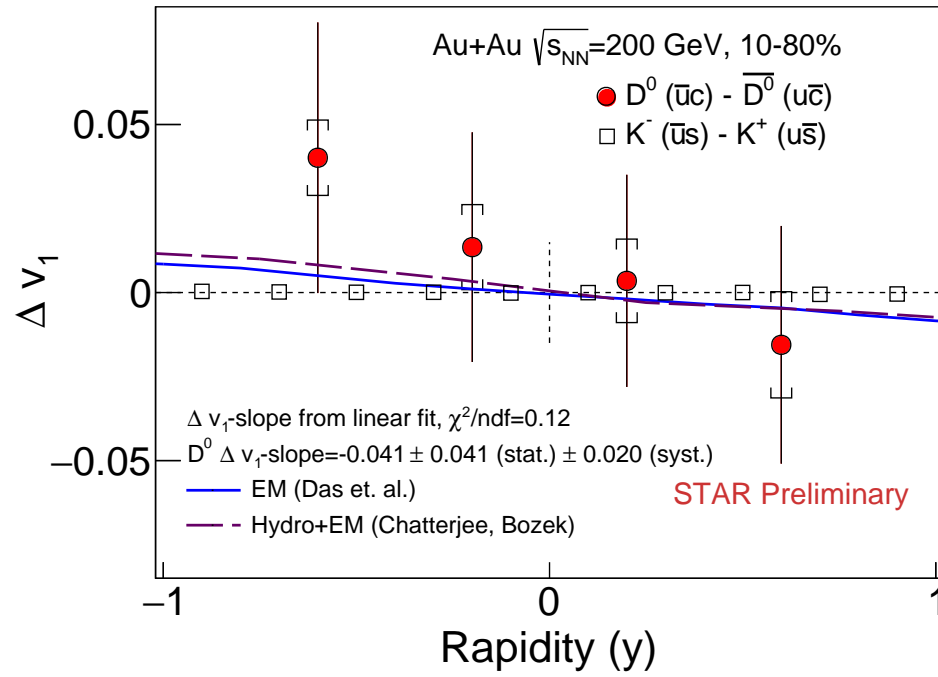
Figure 4.16. The red circles represent the difference in v_1 (Δv_1) between D^0 and $\bar{D}^0$. The open squares are for Δv_1 between K^- and K^+ mesons. The blue solid line and magenta dashed line are D meson Δv_1 predictions from the initial electromagnetic field only and from hydrodynamics combined with the initial electromagnetic field, respectively.

5. D^0 ELLIPTIC FLOW (V_2)

5.1 Two-Particle Q-Cumulant Method

$D^0 v_2$ is calculated using the two-particle correlation method [43,44]. The methodology is based on Eq. (5.1). For each D^0 candidate, we sum up $\sum_i \cos(2\phi_{D^0} - 2\phi_{hadron_i})$, i denotes the index of hadrons in one certain event, in the same event. We then sum over all D^0 candidates in all events. Finally, divide a total sum by the total number of D^0-hadron pairs in all events to get $\langle \cos(2\phi_D - 2\phi_h) \rangle$:

$$
\begin{aligned}
V_2^{D \cdot h} &\equiv \langle \cos(2\phi_D - 2\phi_h) \rangle \\
&= \langle \cos(2\phi_D - 2\psi_{EP}) \rangle \cdot \langle \cos(2\phi_h - 2\psi_{EP}) \rangle \\
&= v_2^D \cdot v_2^h.
\end{aligned}
\tag{5.1}
$$

Eq. (5.1) is used to determine the product of v_2^D and v_2^h. Using the same method but for the correlation of charged hadrons, v_2^h can be obtained. For the different D^0 p_T range, the unlike-sign $K\pi$ pairs in mass window are used as foreground; the side-bands (both like-sign and unlike-sign) and like-sign in D^0 mass window pairs are used as background.

In the analysis, we used the Q-cumulant method [25] as Eq. (5.2). The Q value is calculated D^0-by-D^0 as

$$
Q = \frac{\cos(2\phi_D) \cdot \sum_h \cos(2\phi) + \sin(2\phi_D) \cdot \sum_h \sin(2\phi)}{N_h}
\tag{5.2}
$$
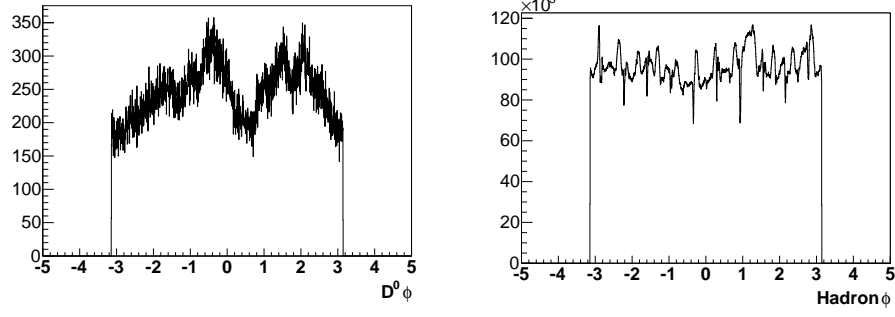
Figure 5.1. The ϕ distribution of D^0 candidates and charged hadrons. The left panel shows the ϕ distribution of D^0 candidates. The right panel shows the ϕ distribution of primary tracks in $|\eta| < 1$.

The final correlation $v_2^{D \cdot h}$ is the weighted average value of the cumulant. The weight w_i is defined as the product of 1) the number of hadrons correlated to the D^0, 2) the centrality weights of the VPD trigger and 3) the reverse of the D^0 reconstruction efficiency.

$$V_2^{D \cdot h} \equiv \langle \cos(2\phi_D - 2\phi_h) \rangle = \frac{\sum\limits_{D^0} w_i \cdot Q}{\sum\limits_{D^0} w_i} \tag{5.3}$$

5.2 Non-uniform Acceptance Correction

The azimuthal angle ϕ distribution should be flat for a perfect detector. However, in the experiments, the detectors may have a non-uniform acceptance which can lead to anisotropic distributions in the lab frame. In Figure 5.1, the non-flat ϕ distribution is because of the detector acceptance, which introduces a bias into the v_2 calculation. In the two-particle correlation analysis, Eq. (5.4) is used to fix the non-uniform acceptance by subtracting the respective averages of the two terms in the calculation of two-particle correlation, Eq. (5.1) [25]. In Eq. (5.4), the $\langle \cos(2\phi_D - 2\phi_h) \rangle$ term is calculated using weighted D^0 cumulant. The correction, for example the $\langle \sin(2\phi_h) \rangle$ term, is the averaged value of hadrons used in the correlation.

$$V_2^{D \cdot h} = \langle \cos(2\phi_D - 2\phi_h) \rangle - \langle \cos(2\phi_D) \rangle \cdot \langle \cos(2\phi_h) \rangle - \langle \sin(2\phi_D) \rangle \cdot \langle \sin(2\phi_h) \rangle \quad (5.4)$$
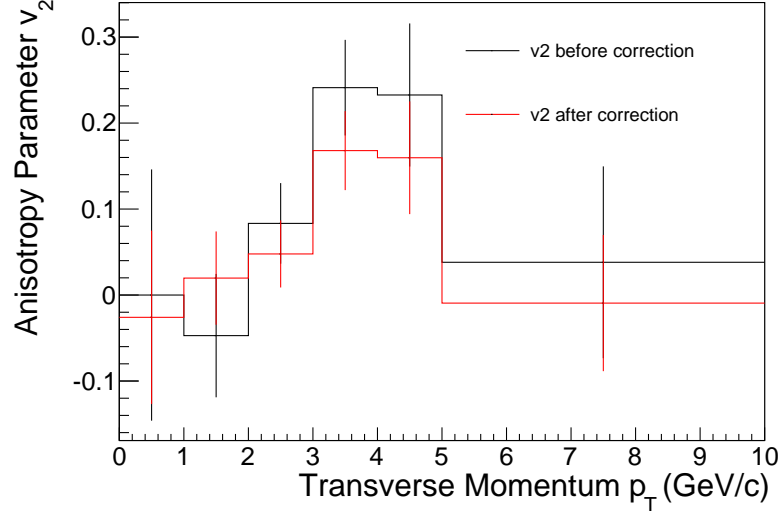
Figure 5.2. D^0 v_2 before and after the fixing of the non-uniform acceptance of detector

Figure. 5.2 shows the D^0 v_2 before and after fixing the non-uniform acceptance. In order to reduce the anisotropy from now-flow effect, $\Delta\eta$ between the D^0 candidates and the hadrons is required. In this analysis, the traditional η-sub event procedure is applied. Figure 5.3 shows the scheme of the η-sub procedure. The D^0 candidates are correlated with the tracks from the opposite half of the TPC. Tracks within $|\eta| < 0.05$ are always removed to provide a minimum η gap between the D^0 and other charged hadrons.

5.2.1 Reference Hadron v_2

The reference hadron v_2 is calculated in Eq. 5.5.

$$(v_2^h)^2 = \langle \cos(2\phi_{h1} - 2\phi_{h2}) \rangle. \quad (5.5)$$
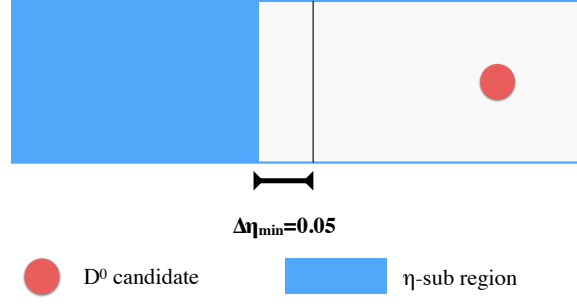
Figure 5.3. Scheme of η-sub event procedure.

For each event, we split all hadrons into two groups based on the TPC η region and calculate the cumulant for each group. We then calculate the weighted average values of the product of the two cumulants in each event. The hadron v_2 is calculated using

$$
v_2^h = \sqrt{\frac{\sum\limits_{events} \left(\sum\limits_{left} \cos(2\phi) \cdot \sum\limits_{right} \cos(2\phi) + \sum\limits_{left} \sin(2\phi) \cdot \sum\limits_{right} \sin(2\phi) \right)}{\sum\limits_{event} N_{hadron}^{left} \cdot N_{hadron}^{right}}}
\tag{5.6}
$$

Similarly as in the calculation of D^0 v_1, a rapidity gap of $\Delta\eta > 0.05$ between the two groups is required in hadron v_2 calculation as well for two reasons. First, to suppress the non-flow effects between hadrons; and second, to suppress the track merging due to two close tracking merging to one in the track reconstruction.

The hadron v_2 obtained with cumulant method in this thesis work is compared in Fig. 5.4 with previous analysis with Run-10 data [45]. The method used in Run-10 analysis was to loop over all particles twice and calculate the angular correlation. We expected smaller v_2 from cumulant method due to suppressed non-flow effects with η-gap imposed. But in very central events, the v_2 is similar from both methods; which might be due to track merging. When two tracks are very close to each other are reconstructed as one, the very

Table 5.1. Reference hadron v_2 in different centrality bins.

centrality	hadron v_2 %	error of hadron v_2 %
$0 - 5\%$	2.5525	0.0008
$5 - 10\%$	3.6077	0.0008
$10 - 20\%$	5.0554	0.0006
$20 - 30\%$	6.5654	0.0007
$30 - 40\%$	7.4101	0.0008
$40 - 50\%$	7.6407	0.0011
$50 - 60\%$	7.3495	0.0016
$60 - 70\%$	6.7478	0.0032
$70 - 80\%$	6.2187	0.0080

strong correlation between them is not counted, and this will decrease the measured v_2. This effect is not present when a sufficient η gap is applied.
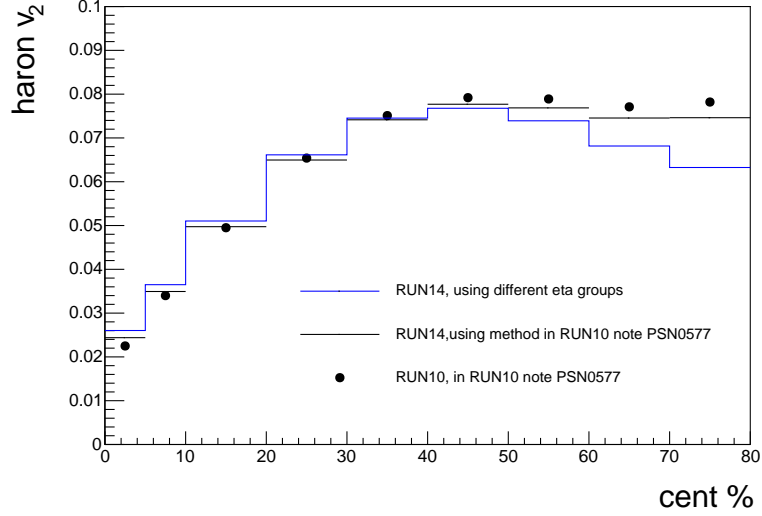
Figure 5.4. Comparison between Run 14 and Run 10 hadron v_2 measurements. The black dots present the result in analysis note using Run-10 data. The black line uses same method in the analysis note with Run-14 data. The blue line uses cumulant method with Run-14 data.

5.3 Signal Extraction

Eq. (5.1) is used to get the v_2 of D^0 candidates. Then Eq. (5.7) is used to subtract the background. N_{cand} is the yield of unlike-sign $K\pi$ pair in 3σ within the mass window where σ is the square root of variance from the fitting Gaussian function. N_{sig} is the fitting result, and $N_{bkg} = N_{cand} - N_{sig}$. The D^0 candidate v_2 (v_2^{cand}), also comes from the correlation of unlike-sign pair in 3σ mass window to the hadrons. In two-particle correlation method, the η gap between D^0 and hadrons can be applied. In this way, the effect of non-flow can be suppressed effectively. The left panel of Fig. 5.5 shows the correlation ($cos(2\phi_D - 2\phi_{hadron})$) as a function of p_T.

The v_2^{bkg} comes from 1) like-sign pairs in the mass window ($\pm3\sigma$); 2) like-sign pairs in side bands, and 3) unlike-sign pairs side bands. These three samples include almost
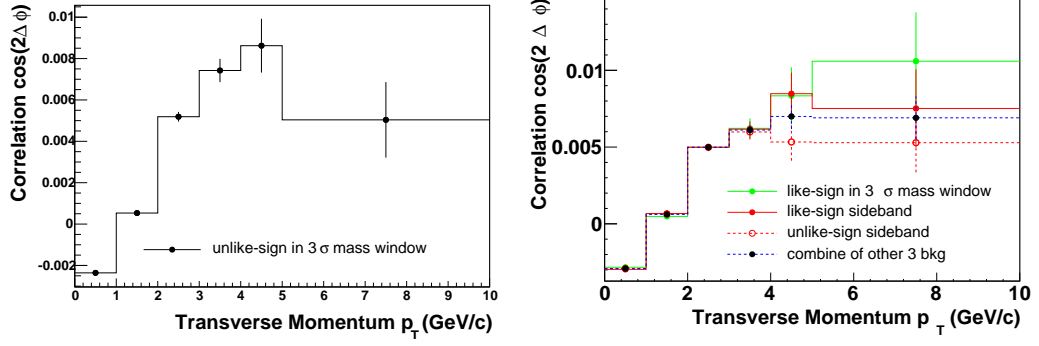
Figure 5.5. v_2 as a function of p_T for D^0 candidates(left) and backgrounds(right). In the backgrounds plot, the three color lines are from different $K\pi$ pair samples. The blue line is the weighted average of them.

all combinations for the best statistic, so we can use them as background. However, both the unlike-sign and side-band backgrounds are biased. The like-sign pairs cannot describe background in unlike-sign pairs due to different combinatorial background components; while the double-counting ratios in the D^0 mass window and side-bands region are different.

$$v_2^{sig} = \frac{N_{cand} \cdot v_2^{cand} - N_{bkg} \cdot v_2^{bkg}}{N_{signal}} \tag{5.7}$$

The right panel of Fig. 5.5 shows results from different background samples. The black dots show the weighted average value of the three background samples, which is the default value used in the v_2 calculation. The maximum difference between the three samples and the default background v_2 is considered as a systematic uncertainty.

We have v_2^{cand}, v_2^{bkg}, N_{cand}, N_{bkg} and N_{sig} in the Eq. (5.7) to calculate D^0 v_2. The v_2 of candidates and backgrounds, which is the mean value of $\cos(2\phi)$, is calculated using the TProfile class in ROOT. The uncertainty of v_2 is offered by TProfile. The uncertainty of N_{cand} is $\sqrt{N_{cand}}$. The value of the N_{sig} comes from fitting, so the fitting error is included in the number N_{sig}. Finally, assuming N_{sig}, N_{cand} and v_2 are not related to each other,

the statistical uncertainty is as in Eq. 5.8. Since the uncertainty of v_2 is related to the number of candidates, the uncertainty calculated in this way might be over-estimated. But the uncertainty introduced by N_{cand} and N_{signal} are negligible.

$$v_2^{sig} = \frac{N_{cand} \cdot v_2^{cand} - N_{bkg} \cdot v_2^{bkg}}{N_{signal}}$$

$$= \frac{N_{cand}}{N_{signal}} \cdot v_2^{cand} + (1 - \frac{N_{cand}}{N_{signal}}) \cdot v_2^{bkg}$$

$$\sigma(v_2^{sig}) = \sqrt{((v_2^{cand} - v_2^{bkg}) \cdot \sigma(\frac{N_{cand}}{N_{signal}}))^2 + (\frac{N_{cand}}{N_{signal}} \cdot \sigma(v_2^{cand}))^2 + ((1 - \frac{N_{cand}}{N_{signal}}) \cdot \sigma(v_2^{bkg}))^2}$$

$$(5.8)$$

Table 5.2. Candidate and background yields and V_2 in different p_T bins.

D^0 p_T	$N_{Candidate}$	N_{Signal}	$V_2^{candidate}$	$V_2^{background}$	$v_2^{D^0}$
0-1 GeV/c	859030±861.70	8936.6±1046.54	-0.00286±0.00003	-0.00289±0.00003	0.0043±0.1789)
1-2 GeV/c	317965±527.17	13062.4±622.88	0.00051±0.00005	0.00061±0.00005	-0.0475±0.0739
2-3 GeV/c	51610.4±213.80	7112.81±254.71	0.00504±0.00011	0.00496±0.00011	0.1253±0.0459
3-4 GeV/c	9311.33±92.27	2609.28±106.53	0.00718±0.00030	0.00617±0.00030	0.2174±0.0519
4-5 GeV/c	2227.26±45.83	977.97±53.50	0.00704±0.00079	0.00724±0.00079	0.1400±0.0720
5-10 GeV/c	1509.08±38.56	734.82±44.88	0.00449±0.00134	0.00694±0.00134	0.0241±0.0875

5.4   Systematic Uncertainties

In this analysis, three different systematic uncertainties are considered. The first one is the uncertainty of D^0 yield. The default method uses second order polynomial to describe the background invariance mass distribution. To estimated the uncertainty, an exponential function is used as reference to compare with the default value. The difference, translated to D^0 v_2 is considered as the first systematic uncertainty.

The second source of systematic uncertainty comes from background v_2 estimation. As mentioned before, we choose side-band of like-sign, unlike-sign pairs, also like-sign pairs in D^0 mass window as different background estimations and the average value as the

default value used for the D^0 v_2 calculation. Also, the topological cuts with 50% and 150% D^0 yields are used for estimated the systematic background. Fig. 5.6 shows the v_2 results with different backgrounds and different topological cuts. Assuming the v_2 from all these combinations form a uniform distribution, the mean square root error can be obtained as the maximum differences among all combinations divided by $\sqrt{12}$. This is quoted as the systematic error of the measured v_2, similarly to what is done in the event plane method.
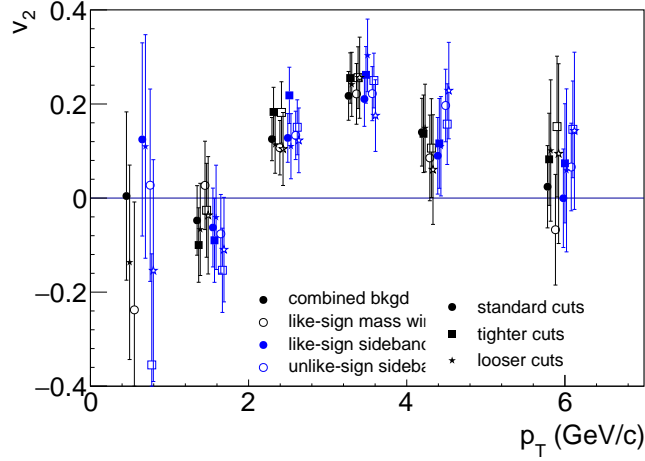
Figure 5.6. v_2 vs. p_T with different backgrounds and topological cuts .

Just like in event plane method, the inverse D^0 reconstruction efficiency uncertainty is the third systematic uncertainty. Fig. 5.7 shows D^0 v_2 with and without inverse D^0 reconstruction efficiency. The difference between the two values is a conservative estimation of this systematic uncertainty.

Table 5.3 summarizes D^0 p_T, v_2, v_2 statistical error, two v_2 systematic error components, and the total v_2 systematic error.

5.5   Results and Discussion

Figure 5.8 shows our final results of the D^0 v_2 in 0–80% centrality Au+Au events as a function of p_T using the event plane and correlation methods. The results are consistent with each other within uncertainties.
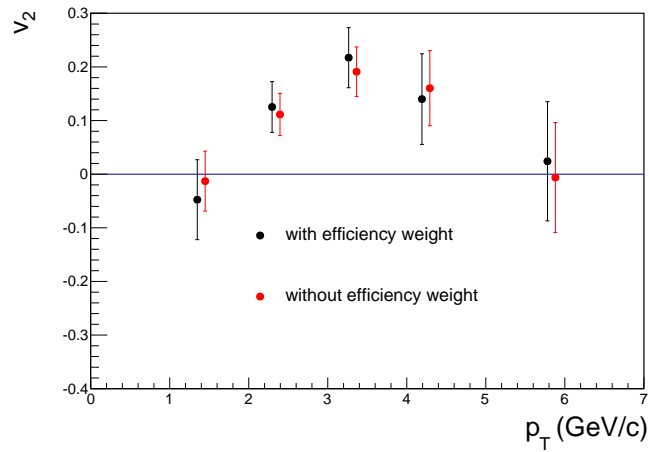
Figure 5.7. v_2 vs. p_T with and without inverse D^0 reconstruction efficiency weight .
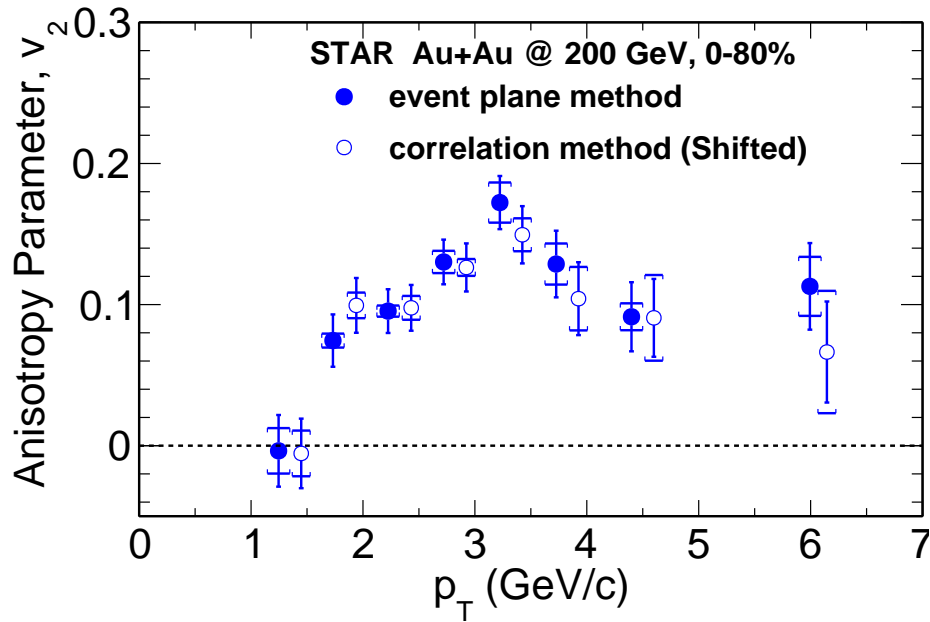
Figure 5.8. v_2 as a function of p_T for D^0 extracted with the event plane and correlation methods for 0–80% centrality Au+Au collisions at $\sqrt{s_{NN}} = 200$ GeV. The vertical bars and brackets represent the statistical and systematic uncertainties, respectively. The open points are shifted along x-axis for clarity.
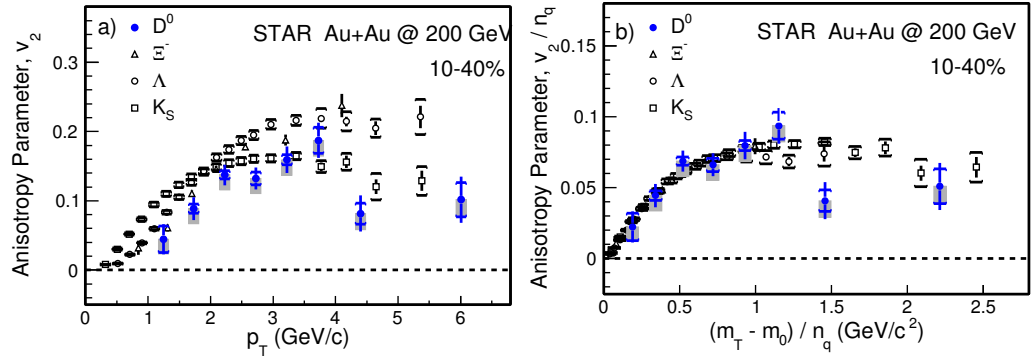
Figure 5.9. (color online) (a) v_2 as a function of p_T and (b) v_2/n_q as a function of $(m_T - m_0)/n_q$ for D^0 in 10–40% centrality Au+Au collisions compared with K_S^0, Λ, and Ξ^- [46]. The vertical bars and brackets represent statistical and systematic uncertainties, and the grey bands represent the estimated non-flow contribution.

Figure 5.9 compares the measured D^0 v_2 from the event plane method in the 10–40% centrality bin with the v_2 of K_S^0, Λ, and Ξ^- particles. Panel (a) shows v_2 as a function of p_T, where a clear mass ordering for $p_T < 2\,\text{GeV}/c$ including D^0 is observed. For $p_T > 2\,\text{GeV}/c$, the D^0 v_2 follows the v_2 of other light mesons [46–48]. Panel (b) shows v_2/n_q as a function of $(m_T - m_0)/n_q$, where n_q is the number of constituent quarks (NCQ) in the hadron, m_0 the rest mass, and $m_T = \sqrt{p_T^2 + m_0^2}$. We find that the D^0 v_2 falls onto the same universal trend as all other light hadrons. This suggests that charm quarks have gained flow through interactions with the sQGP medium in 10–40% Au+Au central collisions at $\sqrt{s_{\text{NN}}} = 200\,\text{GeV}$.
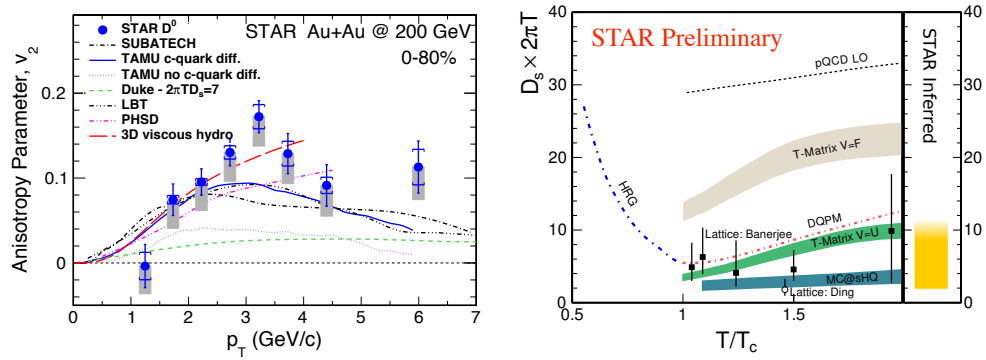
Figure 5.10. (a) Comparison of the measured D^0 v_2 to model calculations; (b) Charm quark diffusion coefficient from model calculations and the inferred range from STAR measurements.

Table 5.3. D^0 p_T, v_2, v_2 statistical error, v_2 systematic error from different fitting functions, different backgrounds, topological cuts, v_2 systematic error from inverse D^0 reconstruction efficiency weight, and total v_2 systematic error.

D^0 p_T (GeV/c)	0.63	1.52	2.47	3.43	4.36	5.95
v_2	0.0043	−0.0475	0.1253	0.2174	0.1400	0.0241
v_2 statistical error	0.1789	0.0739	0.0459	0.0519	0.0720	0.0875
systematics (fitting yields)	N/A	0.0024	0.0000	0.0016	0.0011	0.0099
systematics (backgrounds, cuts)	0.2207	0.0306	0.0362	0.0627	0.0404	0.0369
systematics (inverse efficiency weight)	N/A	0.0346	0.0140	0.0263	0.0204	0.0304
total v_2 systematic error	0.2207	0.0462	0.0388	0.0680	0.0453	0.0486

In Fig. 5.10, left panel, the measured D^0 v_2 in 0–80% centrality bin is compared with several model calculations with different treatments of the charm-medium interaction and thus different values of the charm diffusion coefficient $2\pi T D_s$. The v_2 predicted by the TAMU model with no charm quark diffusion is different from our measurement, while the same model with charm quark diffusion describes the data better [49, 50]. A three-dimensional viscous event-by-event hydrodynamic simulation with viscosity $\eta/s = 0.12$, using the AMPT (A Multi-Phase Transport Model) initial condition and tuned to describe v_2 for light hadrons, predicts D^0 v_2 that is consistent with our data for $p_\mathrm{T} < 4\,\mathrm{GeV}/c$ [51]. This suggests that charm quarks may have achieved thermal equilibrium in these collisions, or get close to thermal equilibrium. In general, several models with a temperature–dependent charm diffusion coefficient $2\pi T D_s$ in the range of $\sim$2–12 for $1 < T/T_c < 2$ are consistent with our measurement. The $2\pi T D_s$ predicted by lattice QCD calculations falls in the same range [52, 53], as shown in the right panel of Fig. 5.10.

6. SUMMARY

In this thesis, I have reported on the measurement of the rapidity-odd directed flow (v_1) as a function of rapidity (y) for D^0 and $\bar{D}^0$ mesons, respectively, in 10-80% central Au+Au collisions at $\sqrt{s_{\mathrm{NN}}} = 200\,\mathrm{GeV}$ using the STAR detector at RHIC. The heavy flavor tracker(HFT) was installed, specifically to reconstruct D^0 and $\overline{D^0}$ mesons. The measured v_1-slope (dv_1/dy) is about 20 times larger than that of kaons with a 3σ significance. This indicates a strong interaction between charm quarks and the initially tilted source created in heavy-ion collisions. Negative dv_1/dy slopes for D^0 and $\bar{D}^0$ are observed to be consistent with predictions from theoretical calculations. The current measurement precision is not sufficient to draw firm conclusions about the splitting between D^0 and $\bar{D}^0$ v_1, which is possible induced by the initial electromagnetic field.

I have also reported the measurement of D^0 elliptic flow(v_2). The measured D^0 v_2 follows the mass ordering at low p_{T} observed for light hadrons. The nunber of constituent quarks (NCQ) scaled v_2 of D^0 is consistent with that of light hadrons for $(m_{\mathrm{T}} - m_0)/n_q < 1\,\mathrm{GeV}/c^2$ in 10–40% (0–80%) central collisions. A three-dimensional viscous hydrodynamic model describes the D^0 v_2 for well $p_{\mathrm{T}} < 4\,\mathrm{GeV}/c$. The results suggest that charm local quarks exhibit the same strong collective behavior as light quarks, and may be close to thermal equilibrium in Au+Au collisions at $\sqrt{s_{\mathrm{NN}}} = 200\,\mathrm{GeV}$. Several theoretical calculations with temperature–dependent, dimensionless charm quark spatial diffusion coefficients ($2\pi T D_s$) in the range of $\sim$2–12 can reproduce the D^0 v_2 result. The charm quark diffusion coefficient from lattice QCD calculations falls in the same range.

The work documented in this thesis constitutes an important part of the STAR heavy flavor physics program. The results obtained by this thesis have helped further our understanding of the properties of the quark-gluon plasma created in heavy-ion collisions at RHIC.

REFERENCES

[1] Murray Gell-Mann. A Schematic Model of Baryons and Mesons. *Phys. Lett.*, 8:214–215, 1964.

[2] G. Zweig. An SU(3) model for strong interaction symmetry and its breaking. Version 2. In D.B. Lichtenberg and Simon Peter Rosen, editors, *DEVELOPMENTS IN THE QUARK THEORY OF HADRONS. VOL. 1. 1964 - 1978*, pages 22–101. 1964.

[3] Elliott D. Bloom et al. High-Energy Inelastic e p Scattering at 6-Degrees and 10-Degrees. *Phys. Rev. Lett.*, 23:930–934, 1969.

[4] R. P. Feynman. The behavior of hadron collisions at extreme energies. *Conf. Proc.*, C690905:237–258, 1969.

[5] William A. Bardeen, H. Fritzsch, and Murray Gell-Mann. Light cone current algebra, π^0 decay, and e^+e^- annihilation. In *Topical Meeting on the Outlook for Broken Conformal Symmetry in Elementary Particle Physics Frascati, Italy, May 4-5, 1972*, 1972.

[6] David J. Gross. Nobel lecture: The discovery of asymptotic freedom and the emergence of qcd. *Rev. Mod. Phys.*, 77:837–849, Sep 2005.

[7] Frank Wilczek. QCD made simple. *Phys. Today*, 53N8:22–28, 2000.

[8] Michael E. Peskin and Daniel V. Schroeder. *An Introduction to quantum field theory*. Addison-Wesley, Reading, USA, 1995.

[9] et al Beringer. Review of particle physics. *Phys. Rev. D*, 86:010001, Jul 2012.

[10] A.H. Mueller. Perturbative qcd at high energies. *Physics Reports*, 73(4):237 – 368, 1981.

[11] A. Majumder and M. Van Leeuwen. The Theory and Phenomenology of Perturbative QCD Based Jet Quenching. *Prog. Part. Nucl. Phys.*, 66:41–92, 2011.

[12] Rajan Gupta. Introduction to lattice QCD: Course. In *Probing the standard model of particle interactions. Proceedings, Summer School in Theoretical Physics, NATO Advanced Study Institute, 68th session, Les Houches, France, July 28-September 5, 1997. Pt. 1, 2*, pages 83–219, 1997.

[13] John Adams et al. Experimental and theoretical challenges in the search for the quark gluon plasma: The STAR Collaboration's critical assessment of the evidence from RHIC collisions. *Nucl. Phys.*, A757:102–183, 2005.

[14] K. Adcox et al. Formation of dense partonic matter in relativistic nucleus-nucleus collisions at RHIC: Experimental evaluation by the PHENIX collaboration. *Nucl. Phys.*, A757:184–283, 2005.

[15] I. Arsene et al. Quark gluon plasma and color glass condensate at RHIC: The Perspective from the BRAHMS experiment. *Nucl. Phys.*, A757:1–27, 2005.

[16] B. B. Back et al. The PHOBOS perspective on discoveries at RHIC. *Nucl. Phys.*, A757:28–101, 2005.

[17] Ranbir Singh, Lokesh Kumar, Pawan Kumar Netrakanti, and Bedangadas Mohanty. Selected Experimental Results from Heavy Ion Collisions at LHC. *Adv. High Energy Phys.*, 2013:761474, 2013.

[18] Gines Martinez. Advances in Quark Gluon Plasma. 2013.

[19] P. Kovtun, Dan T. Son, and Andrei O. Starinets. Viscosity in strongly interacting quantum field theories from black hole physics. *Phys. Rev. Lett.*, 94:111601, 2005.

[20] The Frontiers of Nuclear Science, A Long Range Plan. 2008.

[21] Edmond Iancu and Raju Venugopalan. The Color glass condensate and high-energy scattering in QCD. In Rudolph C. Hwa and Xin-Nian Wang, editors, *Quark-gluon plasma 4*, pages 249–3363. 2003.

[22] Ralf Rapp and Hendrik van Hees. 2008.

[23] Jean-Yves Ollitrault. Anisotropy as a signature of transverse collective flow. *Phys. Rev. D*, 46:229–245, Jul 1992.

[24] A. M. Poskanzer and S. A. Voloshin. Methods for analyzing anisotropic flow in relativistic nuclear collisions. *Phys. Rev. C*, 58:1671–1678, Sep 1998.

[25] Ante Bilandzic, Raimond Snellings, and Sergei Voloshin. Flow analysis with cumulants: Direct calculations. *Phys. Rev. C*, 83:044913, Apr 2011.

[26] Piotr Bozek and Iwona Wyskiel. Directed flow in ultrarelativistic heavy-ion collisions. *Phys. Rev.*, C81:054902, 2010.

[27] J. Brachmann, S. Soff, A. Dumitru, Horst Stoecker, J. A. Maruhn, W. Greiner, L. V. Bravina, and D. H. Rischke. Antiflow of nucleons at the softest point of the EoS. *Phys. Rev.*, C61:024909, 2000.

[28] Sandeep Chatterjee and Piotr Bozek. Interplay of drag by hot matter and electromagnetic force on the directed flow of heavy quarks. 2018.

[29] Santosh K. Das, Salvatore Plumari, Sandeep Chatterjee, Jane Alam, Francesco Scardina, and Vincenzo Greco. Directed Flow of Charm Quarks as a Witness of the Initial Strong Magnetic Field in Ultra-Relativistic Heavy Ion Collisions. *Phys. Lett.*, B768:260–264, 2017.

[30] Umut Gursoy, Dmitri Kharzeev, and Krishna Rajagopal. Magnetohydrodynamics, charged currents and directed flow in heavy ion collisions. *Phys. Rev.*, C89(5):054905, 2014.

[31] K.H. Ackermann et al. Star detector overview. *Nuclear Instruments and Methods in Physics Research Section A: Accelerators, Spectrometers, Detectors and Associated Equipment*, 499(2):624 – 632, 2003. The Relativistic Heavy Ion Collider Project: RHIC and its Detectors.

[32] H. Hahn et al. *Nucl. Instrum. Meth.*, A499:245–263, 2003.

[33] M. Anderson et al. The Star time projection chamber: A Unique tool for studying high multiplicity events at RHIC. *Nucl. Instrum. Meth.*, A499:659–678, 2003.

[34] Yi Wang, Qiunan Zhang, Dong Han, Fuyue Wang, Yancheng Yu, Pengfei Lyu, and Yuanjing Li. Status of technology of mrpc time of flight system. 05 2018.

[35] Joachim Schambach et al. The STAR Heavy Flavor Tracker (HFT). In *Proceedings, 20th International Conference on Particles and Nuclei (PANIC 14): Hamburg, Germany, August 24-29, 2014*, pages 659–664, 2014.

[36] C Adler, A Denisov, E Garcia, M Murray, H Stroebele, and S White. The rhic zero degree calorimeters. *Nuclear Instruments and Methods in Physics Research Section A: Accelerators, Spectrometers, Detectors and Associated Equipment*, 470(3):488 – 499, 2001.

[37] B. I. Abelev et al. Identified particle production, azimuthal anisotropy, and interferometry measurements in Au+Au collisions at s(NN)**(1/2) = 9.2- GeV. *Phys. Rev.*, C81:024911, 2010.

[38] `https://drupal.star.bnl.gov/STAR/blog/rksooraj/good-run-lists-hft-embedding`.

[39] Run 2014 D^0 v_2 analysis note, STAR Note psn0651. `https://drupal.star.bnl.gov/STAR/system/files/note_6.pdf`.

[40] Run 2014 D^0 spectra, R_{AA} analysis note, STAR Note psn0692. `https://drupal.star.bnl.gov/STAR/system/files/2018_0507_D0spectra_Note.pdf`.

[41] Gang Wang Phd Thesis. `https://drupal.star.bnl.gov/STAR/theses/ph-d/gang-wang`.

[42] Leszek Adamczyk et al. Beam-Energy Dependence of Directed Flow of Λ, $\bar{\Lambda}$, $K^{\pm}$, K_s^0 and ϕ in Au+Au Collisions. *Phys. Rev. Lett.*, 120(6):062301, 2018.

[43] Nicolas Borghini, Phuong Mai Dinh, and Jean-Yves Ollitrault. *Phys. Rev.*, C63:054906, 2001.

[44] Ante Bilandzic, Raimond Snellings, and Sergei Voloshin. *Phys. Rev.*, C83:044913, 2011.

[45] `https://drupal.star.bnl.gov/STAR/starnotes/private/psn0577`.

[46] B. I. Abelev et al. *Phys. Rev.*, C77:054901, 2008.

[47] Denes Molnar and Sergei Voloshin. *Phys. Rev. Lett.*, 91:092301, 2003.

[48] L. Adamczyk et al. *Phys. Rev. Lett.*, 116:062301, 2016.

[49] Min He, Rainer J. Fries, and Ralf Rapp. *Phys. Rev.*, C86:014903, 2012.

[50] Min He, Rainer J. Fries, and Ralf Rapp. *Phys. Rev. Lett.*, 110(11):112301, 2013.

[51] Long Gang Pang, Yoshitaka Hatta, Xin Nian Wang, and Bo Wen Xiao. *Phys. Rev.*, D91:074027, 2015.

[52] Debasish Banerjee, Saumen Datta, Rajiv Gavai, and Pushan Majumdar. *Phys. Rev.*, D85:014510, 2012.

[53] Heng Tong Ding, Frithjof Karsch, and Swagato Mukherjee. *Int. J. Mod. Phys.*, E24(10):1530007, 2015.

VITA

Liang He graduate from University of Science and Technology of China (USTC) with a Bachelors of Science Degree in Physics in July 2011. He pursued his Master degree in USTC from 2011 to 2013. He joined ATLAS experiment in the LHC at year 2011 for the measurement of $W\gamma$ and $Z\gamma$ production cross sections in proton–proton collisions at the Large Hadron Collider (LHC). Liang finished his Master in Physics from USTC in July 2013. Liang joined Purdue University graduate school in year 2013. In year 2014, Liang joined STAR experiment at the Relativistic Heavy-Ion Collider, Brookhaven National Lab. Upton, NY. Liang worked on the collective flow of heavy flavors in STAR experiment, including the analysis work presented in this dissertation.